

1 COMPUTING HUBS IN THE HIPPOCAMPUS AND CORTEX

2

3 Wesley Clawson¹, Ana F. Vicente¹, Maëva Ferraris¹, Christophe Bernard^{1,#}, Demian
4 Battaglia^{1,#,*}, Pascale P Quilichini^{1,#,*}

5

6 ¹ Aix Marseille Univ, Inserm, INS, Institut de Neurosciences des Systèmes, Marseille,
7 France

8

9 # equally contributing last authors

10 * corresponding authors [demian.battaglia, pascale.quilichini]@univ-amu.fr]

11

12 Abstract

13

14 **Neural computation, which relies on the active storage and sharing of information,**
15 **occurs within large neuron networks in the highly dynamic context of varying**
16 **brain states. Whether such functions are performed by specific subsets of neurons**
17 **and whether they occur in specific dynamical regimes remains poorly understood.**
18 **Using high density recordings in the hippocampus, medial entorhinal and medial**
19 **prefrontal cortex of the rat, we identify computing substates, or discrete epochs,**
20 **in which specific computing hub neurons perform well defined storage and**
21 **sharing operations in a brain state-dependent manner. We retrieve a multiplicity**
22 **of distinct computing substates within each global brain state, such as REM and**
23 **nonREM sleep. Half of recorded neurons act as computing hubs in at least one**
24 **substate, suggesting that functional roles are not firmly hardwired but**

25 **dynamically reassigned at the second timescale. We identify sequences of substates**
26 **whose temporal organization is dynamic and stands between order and disorder.**
27 **We propose that global brain states constrain the language of neuronal**
28 **computations by regulating the syntactic complexity of these substate sequences.**

29

30 Information processing in the brain can be approached on three different levels:
31 biophysical, algorithmic and behavioral (1). The algorithmic level, which remains the
32 least understood, describes the way in which emergent functional computations can be
33 decomposed into simpler processing steps, with architectures mixing serial and
34 massively parallel aspects (2). At the lowest level of individual system components -
35 here, in single neurons, such building blocks of distributed information processing can
36 be modeled as primitive operations of storing, transferring, or non-linearly integrating
37 information streams (3).

38 In resting state conditions, both BOLD and EEG signals are characterized by discrete
39 epochs of functional connectivity or topographical stability, defined as resting state
40 networks and microstates, respectively (4-5). The transitions between these large-scale
41 epochs are neither periodic nor random but occur through a not yet understood syntax,
42 which is fractal and complex (5). Does such organization at the macroscopic scale
43 (whole brain and networks of networks for resting state networks and microstates,
44 respectively) also exist at the microscopic scale? Said differently, is neuronal activity
45 at the microcircuit level organized in discrete epochs associated to different “styles” of
46 information processing? Our first goal is to determine whether information processing
47 at the local neuronal circuit level is structured into discrete sequences of substates, and
48 whether such sequences have an observable syntax, whose complexity could be a
49 hallmark of computation. Here we focus on low-level computing operations, performed
50 by individual neurons such as basic information storage and sharing (6-7). To reduce

51 external perturbations, such as sensory inputs, and to establish if primitive processing
52 operations and their temporal sequences are brain state-dependent, we study two
53 conditions: anesthesia and natural sleep, which are characterized by alternating stable
54 brains states, theta (THE)/slow oscillations (SO) and rapid eye movement
55 (REM)/nonREM sleep, respectively. We consider the CA1 region of the hippocampus,
56 the medial entorhinal cortex (mEC) and the medial prefrontal cortex (mPFC) to
57 determine whether algorithmic properties are shared between regions with different
58 cytoarchitectures.

59 The second goal is to determine whether primitive processing operations are
60 localized, or on the contrary, distributed within the microcircuit as proposed for
61 attractor neural networks (8) and liquid state machines (9). This raises two key
62 questions: Are certain operations driven by a few key neurons, similar to hub cells in a
63 rich club architecture (10)? and Do neurons have pre-determined computing roles, such
64 as ‘sharer’ or ‘storer’ of information’, as well as rigidly prescribed partners in their
65 functional interactions? Said differently - is information routed through a hardwired
66 ‘neuronal switchboard system’ like in early days of telephony? Or dynamically via
67 different addressable nodes like in decentralized peer-to-peer services?

68 Here we demonstrate the existence of a multiplicity of distinct computing substates
69 at the microcircuit level within each of the probed global brain states in both anesthesia
70 and natural sleep. The low-level algorithmic roles played by individual neurons change
71 from one substate to the other and appear largely independent from the underlying
72 cytoarchitecture, with roughly half of the recorded neurons acting as transient
73 computing hubs. Furthermore, we reveal complexity not only at the level of information
74 processing within each substate but also at the level of how substates are organized into
75 temporal sequences, which are neither regularly predictable nor fully random. Substate

76 sequences display an elaborate syntax in all the probed anatomical regions, whose
77 complexity is systematically modulated by changes in global brain states.

78 Taken together, our findings suggest a more distributed and less hierarchical style of
79 information processing in neuronal microcircuits, more akin to emergent liquid state
80 computation than to pre-programmed processing pipelines.

81

82 **RESULTS**

83 **Analysis design**

84 Neurons were recorded simultaneously from the CA1 region of the hippocampus
85 and the medial entorhinal cortex (mEC) under anesthesia (18 recordings from 16 rats),
86 and from the CA1 region and the medial prefrontal cortex (mPFC) during natural sleep
87 (6 recordings from 3 rats, see Figures 1A, S1 and S2 for more details on recordings).
88 We focus on two elementary processing functions: *information storage*, i.e. how much
89 information a neuron buffers over time that it has previously conveyed, as measured by
90 the active information storage (3); and *information sharing*, i.e. how much a neuron's
91 activity information content is made available to other neurons, as measured by mutual
92 information (see e.g. in 7). We use the term *feature* to discuss the metrics we use; i.e.
93 firing, information storage or sharing (Figure 1B-C). We use the same analysis design
94 for all features. The `FeatureVector(t_a)` contains the values for the descriptive
95 features as measured in window t_a (Figure 1B). For example, for firing features, if 20
96 cells are recorded, `FeatureVector(t_a)` contains 20 values, representing the firing
97 density of each neuron during window t_a . We first correlate feature vectors for a given
98 window pair (t_a, t_b) . Here, a high correlation value means that the two feature vectors
99 are very similar to one another, i.e. that the features measured at t_a are also found at t_b .
100 After, we build a *feature similarity matrix*, a collection of correlation values between
101 feature vectors for all window pairs, organized in time (Figure 1D). A block along the

102 diagonal indicates a stable state for a given feature, e.g., a period over which units fire,
103 store or share information in a consistently preserved pattern. The axes of the similarity
104 matrix represent time, and repetitions of a block structure along a horizontal or vertical
105 line mean that a stable state for a given feature is reoccurring over time. We then use a
106 simple clustering technique to extract different stable states, which we call *substates*,
107 and display their switching behavior during the recording session (Figure 1D). Finally,
108 we define *computing hubs* as neurons that more heavily participate to the buffering
109 (storage hubs) or the funneling (sharing hubs) of information streams (Figure 1D, see
110 Material and Methods). This notion of computing hub generalizes previously
111 introduced notions of “hubness” (25, 26) beyond the ability to synchronize firing
112 toward more general types of influence on information processing.

113

114 **Identification of brain global states**

115 Unsupervised cluster analysis of the spectral features of the fields recorded in the
116 various brain regions allowed a clear identification of typical global oscillatory patterns
117 (Figure S3), which we call *global brain states*. In the following, all brain states are
118 identified by the clustering analysis of field recordings performed in the CA1 region
119 (stratum oriens to stratum lacunosum moleculare). Unsupervised clustering identified
120 two states for anesthesia corresponding to epochs dominated by slow (SO state) and
121 theta (THE state) oscillations; and two states during sleep corresponding to REM vs
122 nonREM episodes.

123

124 **Brain state-dependent firing substates**

125 As subsets of cells tend to fire spontaneously together in stereotypical patterns (11-
126 12), we first analyzed neuronal firing assemblies. Figure S4 shows that the firing rate,
127 the burst index and entrainment by the phase of the ongoing oscillations were brain

128 region- and brain state-dependent as previously reported (13-14). A simple visual
129 inspection of firing behavior revealed the probable existence of different firing sets, as
130 some neurons tended to fire together during certain epochs; with these epochs repeating
131 themselves over time (Figure S5). To quantify this observation, we constructed the
132 feature vectors $\text{Firing}(t_a)$, whose entries are given by the average firing rate of each
133 neuron within the window of analysis t_a . The complex block structure of the similarity
134 matrix revealed a repertoire of state transitions much richer than the one associated to
135 global brain states (Figure 2). In this example, unsupervised clustering revealed a total
136 of six firing substates in mEC (Figure 2A) and five in mPFC (Figure 2D) during THE
137 and REM, respectively, for the two animals. Figure 2B demonstrates that a given brain
138 state was characterized by the switching between different firing substates. Figure 2E
139 shows that a subset of firing substates was shared between brain states, and importantly
140 that the switch from one firing substate state to another did not necessarily coincide
141 with a change in the brain global state (and vice versa). Quantification over all
142 recordings revealed that firing substates occurred 87% of the time during either one of
143 the possible global brain states (Figures 2C and 2F). Substates were found in the mEC,
144 CA1 and mPFC and we found an average of ~5 substates for all brain regions and brain
145 states (Table 1). These results reveal that, although field recordings show stereotyped
146 oscillatory behavior during a given brain state, the firing behavior of neurons display a
147 richer dynamic repertoire. Their activity is compartmentalized in a small number of
148 firing substates, with discrete switching events from one substate to another. The firing
149 substates are brain state and brain region specific, and they are not strictly entrained by
150 the global oscillatory state.

151

152

153

154 **Storage of information is dynamic within a brain state**

155 At any given time, neuronal activity conveys an amount of information that can be
156 measured by Shannon entropy. We first focused on active information storage, which
157 measures the fraction of information carried by a neuron i at a time t that was present
158 in the past activity history of i itself (Figure S6A). For storage features, we extract
159 several substates (6 for the mEC in the animal shown in Figure 3A, and 7 for CA1 in
160 the animal shown in Figure 3D), with an average of ~ 4 states across all animals (Table
161 1). As before, there was no strict alignment between brain state transitions and storage
162 substate transitions (Figures 3A, B and C, E). Yet, brain state specificity of storage
163 states was 80% for all regions (Figures 3C and F and Table 1).

164 Under anesthesia, the absolute storage values were stronger in mEC than in CA1,
165 particularly in layers 3 and 5 of mEC (Figure S7). During natural sleep, however,
166 storage values for CA1 were two orders of magnitude larger than during anesthesia and
167 were as strong as in mPFC (Figure S7). Storage tended to be weaker for all probed
168 regions and layers in THE with respect to SO during anesthesia, but not during natural
169 sleep (Figure S7). Therefore, information storage is dynamically distributed in discrete
170 substates and is brain state- and region-dependent. In particular, the involvement in
171 storage of a neuron could vary substantially along time without being necessarily
172 paralleled by a comparable change in firing rate (Figures 3B and 3E).

173

174 **Information sharing is dynamic within a brain state**

175 A primitive processing operation complementary to information storage is
176 information sharing, providing a pseudo-directed metric of functional connectivity
177 between any two circuit units (7). For each neuron i we quantified both “shared-in” (i
178 acts as a sharing target, with information shared from j neurons’ past activity, Figure
179 S6B) and “shared-out” information (i acts as a sharing source and information is shared

180 to j neurons' future activity). We first constructed the feature vector $\text{Sharing}(t_a)$
181 containing the total amount of information funneled through each given neuron
182 (integrated in- and out-sharing strengths, represented by big arrows in Figure 4A),
183 irrespective of whom the information was being shared with. Since in- and out-sharing
184 strengths were strongly correlated (average Pearson correlation >0.9), we ignored the
185 distinction between in- and out-sharing and speak generically of sharing substates.
186 Representative sharing similarity matrices and state sequences are shown in Figure 4B
187 (top) for mEC during anesthesia and mPFC during sleep and in Figure S8 for CA1.
188 Here, we studied only information sharing within regions, because the number of pairs
189 of simultaneous units in different regions that showed significant sharing was too small
190 to reach robust conclusions. We found ~ 4 sharing substates on average across animals.
191 Sharing states displayed an 86% specificity for a given brain state (Figure 4D, Table
192 1).

193 During anesthesia, we measured a stronger absolute sharing values in CA1 than in
194 mEC, a pattern reversed with respect to storage values, particularly in stratum radiatum
195 (SR) and stratum pyramidale (SP) of CA1, even though mEC layer 5 had a sharing
196 strength comparable to CA1s SR and SP (Figure S9). During natural sleep, the
197 participation to information sharing of SO in CA1 increased by an order of magnitude
198 and was as large as the one of mPFC, notably layer 4 (Figure S9). As for storage, the
199 involvement of a neuron in sharing could vary along time even without corresponding
200 variations of its firing rate (Figures S8B and S8E).

201

202 **Sharing assemblies are “liquid”**

203 The previous analysis is focused on sharing strengths at the single cell level. We then
204 determined with which neurons sharing cells were exchanging information, i.e. the
205 detailed network neighborhood of sharing, or *sharing assembly* (cartoon networks in

206 Figure 4A). Two striking features were apparent. First, both the block structure of the
207 sharing assemblies and the state transition sequences are nearly matching the sharing
208 strength ones (Figure 4B), as evidenced by a relative mutual information value of 98%
209 on average. Second, in contrast to sharing strengths, the blocks in the sharing assembly
210 similarity matrix were of a light blue color, indicating a strong variability of sharing
211 assemblies within a given substate. This phenomenon was quantified by *liquidity*
212 analysis, with liquidity being a measure bounded between 0 and 1, where a value of 0
213 represents an absence of internal variability within a substate and a value of 1
214 representing completely random variability (see *Materials and Methods*). The liquidity
215 values of sharing assemblies for all sharing substates throughout all recordings lied
216 below the diagonal (Figure 4C). This result can be better understood considering the
217 toy examples of Figure 4A. The cartoons represent snapshots at three different, non-
218 sequential times of a given hub neuron in its sharing network environment. The three
219 considered time frames all fall within the same substate, therefore the overall in- and
220 out-sharing strengths, represented by the orange and grey arrows respectively, are
221 constant (meaning stability). However, the sources and targets of the funneled
222 information can widely vary in time (meaning instability). Although the sum of in-
223 going and out-going information remained overall constant within each sharing
224 substate, information was shared over different cell assemblies from one time period to
225 the next. All three brain regions displayed remarkable liquidity in sharing assemblies
226 through all brain states, and liquidity was brain region- and brain state-specific (Figure
227 4C). As reported in Table 2, the largest liquidity was observed for mPFC sharing
228 assemblies during natural sleep (~94%). CA1 displayed a substantial reduction in the
229 liquidity of sharing assemblies when moving from anesthesia to sleep (dropping from
230 ~86% in anesthesia to ~57% in sleep). Finally, as for the other features, information
231 sharing substates were brain state specific (Figure 4D).

232

233 **Loose coordination of substate transitions between brain regions**

234 Single units were recorded simultaneously in two regions (CA1 and mEC; CA1 and
235 mPFC). We thus assessed whether substate transition events in one region matched the
236 transition in the other region. We computed the relative mutual information between
237 substate sequences of a given type (e.g. firing, storage or sharing) observed in one
238 region and the other. We did not find significant differences for these measures across
239 the three features (firing, storage, sharing) and therefore pooled them together. The
240 median relative mutual information between substate transitions in the probed cortical
241 and hippocampal regions was 18% during anesthesia (between mEC and CA1) and 42%
242 during natural sleep (between mPFC and CA1). These levels of coordination between
243 substate sequences denoted a lack of perfect parallelism between transitions in the
244 different regions, but they were still well above chance level (Figure S10). Thus,
245 substate dynamics display some coordination between CA1 and mPFC during sleep
246 (Table 3), which is in keeping with the fact that information exchange occurs between
247 the two regions during sleep (15). The weak coordination under anesthesia suggests that
248 circuits may operate more independently from one another in this condition (but still
249 not completely).

250

251 **A large fraction of cells can act as computing hubs**

252 Functional, effective, and anatomical hub neurons (mostly GABAergic) have been
253 identified in the brain (16). We complement the concept, introducing *storage* and
254 *sharing hubs*, i.e. neurons displaying an elevated storage or sharing values, respectively
255 (see Methods). In contrast to the sparsity of functional, effective, and anatomical hubs,
256 a large fraction of cells acted as a computing hub in at least one substate, as illustrated
257 in Figure 5A. Computing hubs could be recruited across all probed regions and layer

258 locations (Figure 5B and C). As summarized in Figure 5B, the probability of serving as
259 computing hub – storage or sharing confounded – was of 40% or more on average for
260 almost all layers, apart from the, possibly under-sampled, stratum lacunosum
261 moleculare and stratum radiatum in CA1. We observed a general tendency for
262 inhibitory interneurons to have a larger probability to serve as computing hubs than for
263 excitatory cells. This tendency was particularly strong for cortical regions and was
264 notably significant in layer 5 of mEC (during anesthesia) and layer 3 of mPFC (during
265 sleep), for which the probabilities of inhibitory interneurons serving as computing hub
266 in at least one substate approached 70%. The probability of serving as a computing hub
267 at least once was relatively similar when evaluated separately for storage or sharing. In
268 particular, 43% of the neurons serving as a storage hub in a substate could serve as a
269 sharing hub in another substate, but in general, not simultaneously as only 12% of the
270 neurons were “multi-function” hubs.

271 Despite this large flexibility in the dynamic assignment of hub roles, the notion of
272 hub continued to make sense within each individual substate. Within a substate, on
273 average only ~9% of cells acted as hub (storage or sharing pooled), so still a strict “elite”
274 (although not a permanent one but appointed just within the associated state). The set
275 of recruited hubs constituted thus at each time a characteristic fingerprint of the active
276 substates (with only 4% of the substates being “hubless”).

277 We also studied the probability that a computing hub emerged in a given layer
278 (Figure 5C). During anesthesia, all probed layers of CA1 and mEC showed a ~20%
279 uniform probability for a storage and sharing computing hub to emerge. Natural sleep
280 was associated to an enhanced recruitment of computing hubs. The probabilities of hub
281 emergence exceeded ~40% for storage hubs in layer 5 of mPFC and in SP of CA1. The
282 analysis of deep or superficial CA1 SP principal neurons, which are involved in
283 different microcircuits (17-18), did not reveal an intra-layer distribution of computing

284 hubs (not shown). These results suggest that the probability that a neuron serves as
285 computing hub is not correlated to its anatomical region or layer location.

286 Finally, we tested whether computing hubs were characterized by high firing rates.
287 Using the same procedure utilized to extract computing hubs, we found that 62% of the
288 cells were high-firing at least in one firing substate with 70% being putative
289 interneurons. Remarkably, there was a poor overlap between computing hubs and high
290 firing rate cells. Table 3 already shows that storage and sharing substate sequences are
291 only loosely coordinated with firing substate sequences (cf. as well firing rate
292 information in Figures 3B-E and S8B-E). Furthermore, being a high firing rate cell does
293 not guarantee that this cell will also be a computational hub (or the other way around).
294 This is also shown in Figure 5C, where the yellow levels over the histogram bars
295 indicate the fraction of storage and sharing hubs which also happen to be high firing
296 cells. We conclude that a storage hub can have a normal or even smaller than average
297 firing rate .

298

299

300 **The syntax of substate sequences is complex and brain state-dependent**

301 Collectively, our results demonstrate the existence of substate sequences in three
302 different brain regions during anesthesia and natural sleep. Using a linguistics analogy
303 (Figure S11A), we assign a *letter* to each identified substate (represented by a color in
304 the figures). The temporal sequence of substates thus translates into a stream of *letters*.
305 However, if we consider the three features simultaneously, we obtain a stream of 3 letter
306 *words* (Figure S11B). All combinations of possible letters from our 3 features define
307 the *dictionary* of *words* that can be expressed. We represent a stream of *words* as a
308 switching table (Figure 6A). This allows us to explore two aspects of the “neuronal
309 language”: the statistics of the *words* and the statistics of the transitions between the

310 words (the *syntax*). We found that the *words* were mostly (85%) brain state-specific, as
311 expected since the substates *letters* are already brain state-specific (cf. Figures 3C and
312 F, 4D). Although the syntactic rules structuring the production of *words* are unknown,
313 we can quantify their complexity. Algorithmic information theory (19), the minimum
314 description length framework (20) and the Lempel-Ziv method (21) link complexity to
315 the notion of compressibility. As illustrated in Figure 6B, an ordered, regular switching
316 table requires a short description, as a small list of instructions can be written to
317 reproduce the table (e.g. *word D* 100 times, followed by *word B* 88 times, etc.). At the
318 opposite extreme, a completely random switching table would need a lengthy
319 exhaustive description -as many instructions as the length of the table itself. A complex
320 switching table stands between regularity and randomness and requires a description
321 that is compressed, longer than a regular table but shorter than a random table.

322 Figure 6C shows that the syntax was complex (between 0 and 1) for all brain regions
323 and brain states and that THE/REM states were more complex than SO/nonREM states.
324 We added two recordings from mPFC under anesthesia for comparison. Figure 6D
325 shows that the measured complexity was significantly larger than the upper threshold
326 for regularity and significantly smaller than the lower threshold for randomness
327 ($p < 0.05$, Bonferroni Corrected, direct c.i. comparison).

328 Finally, we assessed whether switching from SO to THE or from nonREM to REM
329 increased the complexity. As shown in Figure 6E, the tendency was toward an increase
330 of complexity in all cases, from +30% for mEC during anesthesia and mPFC during
331 anesthesia or sleep to roughly +10% for CA1 during anesthesia or sleep. This relative
332 increase was always significant ($p < 0.05$, Bonferroni Corrected, c.i. comparison) apart
333 from CA1, for which two recordings displayed increased complexity during nonREM
334 sleep. We conclude that the syntax is complex and brain state-dependent.

335

336 **What determines complexity?**

337 We then investigated which factors contribute to complexity. Different durations of
338 *words* may account for variations in complexity. Although *word* dwell times were
339 different by one order of magnitude between anesthesia and sleep with median ~18 min
340 (~10 min 1st quartile, ~28 min 3rd quartile) during anesthesia and ~1.4 min (~1 min 1st
341 quartile, ~2.1 min 3rd quartile) during sleep, complexity values for anesthesia and
342 natural sleep were similar.

343 We also evaluated the burstiness coefficient, B (22), of the stream of *words*. This
344 coefficient ranged between $-1 \leq B \leq 1$, with $B = -1$ corresponding to a perfectly periodic
345 stream of *words*, $B = 0$ to a Poisson train and $B = 1$ to a maximally bursting stream. We
346 found a positive correlation between burstiness and complexity (Figure S11A, $p < 0.01$,
347 Bootstrap c.i). Burstiness was greater during THE/REM (0.15) than during
348 SO/nonREM (0.09 $p = 0.03$, Kruskal-Wallis test), which may contribute to the
349 increased complexity found during THE/REM.

350 The richness of the dictionary also affects complexity (21). We therefore evaluated
351 the Used Dictionary Fraction, i.e. the ratio between the number of observed *words* and
352 the maximum theoretical number of *words*, i.e. the *dictionary*. We find a significant
353 positive correlation between the Used Dictionary Fraction and complexity (Figure
354 S12B, $p < 0.05$, Bootstrap c.i). The richness of the dictionary was greater during
355 THE/REM (21%) than during SO/nonREM (14%, $p = 0.032$, Kruskal-Wallis test),
356 which may also contribute to the increased complexity found during THE/REM.

357 A bivariate linear regression of complexity over burstiness and Used Dictionary
358 Fraction revealed a correlation of 0.62 ($p < 0.05$, Bootstrap c.i) between predicted and
359 observed complexity, demonstrating that complexity is largely explained by burstiness
360 and the Used Dictionary Fraction.

361 Finally, we verified that our results did not depend on the measure of complexity.
362 Redoing analyses using Lempel-Ziv complexity (21), which was previously used to
363 analyze neural activity (23-24), lead to qualitatively equivalent results. Lempel-Ziv
364 complexity also strongly correlated with our measure of complexity (Figure S11C
365 Pearson correlation 0.84, $p < 0.001$, bootstrap c.i.).

366

367 **Discussion**

368 Here we demonstrate two levels of organization of brain activity. At the single cell
369 level, we find that a large proportion of recorded neurons act as computing hubs during
370 discrete time epochs (substates) within a given stable brain state (e.g. REM and
371 nonREM). At the microcircuit level, we find a rich repertoire of computational substates
372 characterized by temporally structured sequences, whose complexity was modulated by
373 the global brain oscillatory state. Such type of organization was shared between three
374 anatomical different brain regions: the hippocampus, the medial entorhinal cortex and
375 the medial prefrontal cortex.

376

377 The “hubness” of a neuron may be determined by fixed features, e.g. an exceptional
378 extension of axonal arborizations (25); a suitable location in the circuit wiring diagram
379 facilitating the control of synchronization (26); or yet, some developmental “droit
380 d’aînesse” (16). During natural sleep and anesthesia, however, we find that >40% of
381 the recorded neurons act as a computational hub during at least one substate, meaning
382 that computing hubs form a rather open and not so elitist club. The computational
383 hubness is dynamic - a neuron acting as a hub in a given substate may not be a hub in
384 a different substate or may swap its nature (e.g. converting from a storage to a sharing
385 hub). The stronger tendency for putative inhibitory cells to serve as hubs (>70%) is in
386 keeping with the known role of GABAergic cells in orchestrating network activity (16,

387 25-26). Furthermore, because our analysis was limited to few brain states, the
388 proportion of putative principal and GABA neurons acting as computational hubs may
389 even be an underestimate. Perhaps all neurons act as computational hubs during specific
390 brain states (including exploration and quiet awakening).

391

392 That hubs share information with ever changing source and target neurons is in
393 apparent contradiction with the existence of sequential firing of cell assemblies in
394 cortical and hippocampal circuits, including during nonREM sleep (11,16, 27-37). Our
395 information-theoretical analyses require the use of at least 5 s long sliding windows,
396 which is not sufficient to detect fast sequences of activation, as replay events occur
397 within 500 ms (38). Interestingly, replay sequences are not strictly stable as they
398 demonstrate inter-cycle variability (39), which may reflect liquidity. The liquid nature
399 of information sharing suggests that neuronal activity is not frozen at fixed-point
400 attractors as in classic artificial neural networks (40) but may be sampling the broad
401 basin of attraction of shallow attractors (8) or higher-dimensional manifolds “at the
402 edge of chaos”, as found in reservoir computing schemes (41-43). In this case,
403 information is shared across extremely volatile assemblies within a given substate. The
404 assembly dynamics are thus “liquid” – i.e. neither frozen into crystallized patterns, nor
405 fully random as in a gas – and are only mildly constrained to robustly maintain the
406 computational role of sharing hubs while preserving entropy of firing patterns, and
407 therefore bandwidth for local computations (44). This preservation of hub function in a
408 heterogeneous and reconfiguring circuit can be seen as a form of homeostasis of the
409 computing role, generalizing the concept of homeostasis of circuit behavior evidenced
410 in invertebrate systems (45-46). While this latter homeostasis preserves the functional
411 level, in our case homeostasis would extend down to the algorithmic level, referring to
412 the three-level hierarchy proposed by Marr & Poggio (1).

413

414 During a “stable” behavior such as resting state, analysis of BOLD and EEG signals
415 consistently revealed the presence of temporal sequences of resting state networks and
416 topographical microstates, respectively (4-5). Here, we find that an analogous switching
417 between discrete states occurs at a completely different scale of microcircuits. During
418 a “stable” oscillatory regime (e.g. theta rhythm), neuronal computation is indeed
419 organized in temporal sequences of computational substates. Interestingly, while field
420 oscillations constrain neuronal firing and neuronal firing produces field oscillations
421 (47), we find only a loose match between the switch from one oscillatory mode to the
422 other and the switch from one substate to the other. Transitions between global states –
423 related to the scale of mesoscale collective dynamics– sometimes anticipate and
424 sometimes follow transitions between firing, storage or sharing substates –related to the
425 scale of microscopic firing dynamics–, as if dynamic changes occurring at either one of
426 the scales had destabilizing effects on the dynamics at the other scale (in both directions,
427 meso- to micro-scale and micro-to meso-scale). The behavior of CA1 cells may reflect
428 specific internal dynamics, not tightly controlled by the CA1 local field which mostly
429 reflects synaptic inputs originating from outside the CA1 region. Importantly, the
430 repertoire of computing substates is brain state specific. Beyond proposals that
431 oscillations are central for the routing of information between regions (47-48), we thus
432 suggest here that global oscillatory states could also organize information processing
433 within local regions by enforcing the use of their own state-specific “languages”
434 (expressed in terms of combinations of alternative intrinsic substates).

435

436 Signatures of computation can be identified even if the function and meaning of the
437 computation are unknown and even when system states are sampled partially, as it is
438 the case for the present study. This allowed us to extract a symbolic representation of

439 substates (*letters*) for a given feature, which make *words* when considering several
440 features. The syntax of the substate word sequences is complex, standing between order
441 and randomness (as it was already the case for the sharing dynamics within each
442 substate). The capacity to generate complex sequences of patterns is a hallmark of self-
443 organizing systems and has been associated to their emergent potential to perform
444 universal computations (70). Moreover, dynamics at the “edge of chaos” confer
445 advantages for information processing (41-43).

446

447 Importantly, we find that the syntactic complexity of substate sequences is brain
448 state-dependent as it was the case for the substate dictionaries, and more complex
449 during theta oscillations/REM sleep than during slow oscillations/nonREM sleep,
450 suggesting an increased load of computation in the former brain state. Remarkably, the
451 temporal complexity of activation sequences was also shown to be modulated by brain
452 states at the macro-scale level of whole-brain dynamics (49). In keeping with the view
453 that slow/theta oscillations measured during anesthesia share general properties with
454 nonREM/REM sleep (50-52), we found similar rules of organization in terms of
455 substate sequences and their complexity, despite the fact that the *word* dwell times in
456 anesthesia are one order of magnitude greater than during natural sleep. We speculate
457 that the nature of the undergoing oscillation (slow vs theta) constrains the repertoire of
458 *words* used and their syntax, modulating the type of computation performed by the
459 recruitment of varying computing hubs. Sleep, oscillatory patterns, and neuronal firing
460 are altered in numerous neurological disorders, including epilepsy (18, 53-56) and
461 therefore it will be important to assess whether the repertoire of substates and the syntax
462 are likewise affected.

463

464 In conclusion, our results reveal a rich algorithmic-level organization of brain
465 computations during natural sleep and anesthesia, which combines a complex
466 combinatorics of discrete states with the flexibility provided by liquidly reconfiguring
467 assemblies. While we cannot yet prove that this substate dynamics is functionally
468 relevant, it has the potential to serve as a substrate for previously undisclosed
469 computations. The next aim will be to perform the similar analysis during specific
470 behavioral tasks, such as goal-driven maze navigation. *Words* and/or their sequence
471 may sign specific cognitive processes. The fact that the algorithmic instructions and
472 primitive processing operations are similar in three brain regions with different
473 architectural organizations suggests the existence of a basic architecture for low-level
474 computations shared by diverse neuronal circuits.

475

476 **Acknowledgements**

477 We used part of the data collected in G. Buzsáki's laboratory and originally published
478 by Quilichini et al. (2010) for our investigations. We acknowledge G. Buzsáki and A.
479 Sirota for consenting to the use of this database in the present work. We also used part
480 of the data originally published by Ferraris et al. (2018). PPQ acknowledges support
481 from FRM, FFRE and CURE Epilepsy Taking Flight Award. MF acknowledges
482 support from FRM. The M-GATE project has received funding from the European
483 Union's Horizon 2020 research and innovation program under the Marie Skłodowska-
484 Curie grant agreement No 765549. DB acknowledges support by the CNRS "Mission
485 pour l'Interdisciplinarité" INFINITI program (BrainTime) and the French Agence
486 Nationale pour la Recherche (ERMUNDY, ANR-18-CE37-0014-02). The funders had
487 no role in study design, data collection and analysis, decision to publish, or preparation
488 of the manuscript. We wish also to acknowledge Viktor Jirsa, Lionel Barnett and Thilo
489 Womelsdorf for constructive comments.

490

491

492 **References**

- 493 1. Marr D, Poggio T (1976) From understanding computation to understanding neural
494 circuitry. MIT A.I. Memo 357
- 495 2. Zylberberg A, Dehaene S, Roelfsema PR, Sigman M (2011) The human Turing
496 machine: a neural framework for mental programs. Trends Cogn Sci (Regul Ed)
497 15(7):293–300.
- 498 3. Lizier JT, Atay FM, Jost J (2012) Information storage, loop motifs, and clustered
499 structure in complex networks. Physical Review E 86(2-2):026110.
- 500 4. Hutchison RM, et al. (2013) Dynamic functional connectivity: promise, issues, and
501 interpretations. NeuroImage 80:360–378.
- 502 5. Michel CM, Koenig T (2018) EEG microstates as a tool for studying the temporal
503 dynamics of whole-brain neuronal networks: A review. Neuroimage 15;180(Pt
504 B):577-593. Review.
- 505 6. Wibral, M., Lizier, J. T., Vögler, S., Priesemann, V., & Galuske, R. (2014). Local
506 active information storage as a tool to understand distributed neural information
507 processing. *Frontiers in Neuroinformatics*,8. doi:10.3389/fninf.2014.00001
- 508 7. Kirst C, Timme M, Battaglia D (2016) Dynamic information routing in complex
509 networks. Nat Comms 7:11061.
- 510 8. Amit D.J. Modeling Brain Function: The World of Attractor Neural Networks.
511 Cambridge University Press, Cambridge, 1992.
- 512 9. Maass W, Natschläger T, Markram H (2002) Real-time computing without stable
513 states: a new framework for neural computation based on perturbations. Neural
514 Comput 14(11):2531–2560.

- 515 10. Shimono M, Beggs JM (2015) Functional Clusters, Hubs, and Communities in the
516 Cortical Microconnectome. *Cerebral Cortex* 25(10):3743–3757.
- 517 11. Luczak A, Barthó P, Harris KD (2009) Spontaneous events outline the realm of
518 possible sensory responses in neocortical populations. *Neuron* 14;62(3):413-25.
- 519 12. Sadovskey AJ, MacLean JN (2014). Mouse visual neocortex supports multiple
520 stereotyped patterns of microcircuit activity. *J Neurosci* 4;34(23):7769-77.
- 521 13. Klausberger T, Magill PJ, Márton LF, Roberts JD, Cobden PM, Buzsáki G,
522 Somogyi P (2003). Brain-state- and cell-type-specific firing of hippocampal
523 interneurons in vivo. *Nature* 421(6925):844-8.
- 524 14. Watson BO, Levenstein D, Greene JP, Gelinás JN, Buzsáki G (2016). Network
525 Homeostasis and State Dynamics of Neocortical Sleep. *Neuron* 90(4):839-52.
- 526 15. Marshall, L. & Born, J. The contribution of sleep to hippocampus-dependent
527 memory consolidation. *Trends in Cognitive Sciences* 11, 442–450 (2007).
- 528 16. Cossart R (2014) Operational hub cells: a morpho-physiologically diverse class of
529 GABAergic neurons united by a common function. *Curr Opin Neurobiol* 26:51–
530 56.
- 531 17. Mizuseki K, Diba K, Pastalkova E, Buzsáki G (2011). Hippocampal CA1 pyramidal
532 cells form functionally distinct sublayers. *Nat Neurosci* 14(9):1174-81.
- 533 18. Valero M, Cid E, Averkin RG, Aguilar J, Sanchez-Aguilera A, Viney TJ, Gomez-
534 Dominguez D, Bellistri E, de la Prida LM (2015) Determinants of different deep
535 and superficial CA1 pyramidal cell dynamics during sharp-wave ripples. *Nat*
536 *Neurosci* 18(9):1281-1290.
- 537 19. Chaitin, G.J. *Algorithmic Information Theory*, Cambridge University Press,
538 Cambridge, 1987.
- 539 20. Rissanen J (1983). A Universal Data Compression System. *IEEE Trans. Inf. Theor.*
540 29:656–664.

- 541 21. Ziv J, Lempel A (1977). A Universal Algorithm for Sequential Data Compression.
542 IEEE Transactions on Information Theory. 23 (3): 337–343.
- 543 22. Holme P, Saramäki J (2012) Temporal networks. Physics reports 519(3):97–125.
- 544 23. Szczepański J, Amigó JM, Wajnryb E, Sanchez-Vives MV (2003) Application of
545 Lempel-Ziv complexity to the analysis of neural discharges. Network 14(2):335–
546 50.
- 547 24. Abásolo D, Simons S, Morgado da Silva R, Tononi G, Vyazovskiy VV (2015)
548 Lempel-Ziv complexity of cortical activity during sleep and waking in rats. J
549 Neurophysiol 113(7):2742–2752.
- 550 25. Bonifazi P, et al. (2009) GABAergic hub neurons orchestrate synchrony in
551 developing hippocampal networks. Science 326(5958):1419–1424.
- 552 26. Quilichini PP et al. (2012) GABA Hub neurons mediate gamma-frequency
553 oscillations at ictal-like event onset in the immature hippocampus. Neuron 74:57-
554 64.
- 555 27. Ikegaya Y, et al. (2004) Synfire chains and cortical songs: temporal modules of
556 cortical activity. Science (New York, NY) 304(5670):559–564.
- 557 28. Jones LM, Fontanini A, Sadacca BF, Miller P, Katz DB (2007) Natural stimuli
558 evoke dynamic sequences of states in sensory cortical ensembles. Proc Natl Acad
559 Sci USA 104(47):18772–18777.
- 560 29. Miller J-EK, Ayzenshtat I, Carrillo-Reid L, Yuste R (2014) Visual stimuli recruit
561 intrinsically generated cortical ensembles. Proc Natl Acad Sci USA
562 111(38):E4053–61.
- 563 30. Tavoni G, Ferrari U, Battaglia FP, Cocco S, Monasson R (2017) Functional
564 coupling networks inferred from prefrontal cortex activity show experience-related
565 effective plasticity. Network Neuroscience 1(3):275–301.

- 566 31. Feldt S, Bonifazi P, Cossart R (2011) Dissecting functional connectivity of neuronal
567 microcircuits: experimental and theoretical insights. *Trends Neurosci* 34(5):225–
568 236.
- 569 32. Skaggs, W. E., & McNaughton, B. L. (1996). Replay of Neuronal Firing
570 Sequences in Rat Hippocampus During Sleep Following Spatial
571 Experience. *Science*, 271 (5257), 1870-1873. doi:10.1126/science.271.5257.1870
- 572 33. Lee, A. K., & Wilson, M. A. (2002). Memory of Sequential Experience in the
573 Hippocampus during Slow Wave Sleep. *Neuron*, 36(6), 1183-1194.
574 doi:10.1016/s0896-6273(02)01096-6
- 575 34. Pastalkova, E., Itskov, V., Amarasingham, A., & Buzsaki, G. (2008). Internally
576 Generated Cell Assembly Sequences in the Rat Hippocampus. *Science*,
577 321(5894), 1322-1327. doi:10.1126/science.1159775
- 578 35. Euston, D. R., Tatsuno, M., & McNaughton, B. L. (2007). Fast-Forward Playback
579 of Recent Memory Sequences in Prefrontal Cortex During Sleep. *Science*,
580 318(5853), 1147-1150. doi:10.1126/science.1148979
- 581 36. Peyrache, A., Khamassi, M., Benchenane, K., Wiener, S. I., & Battaglia, F. P.
582 (2009). Replay of rule-learning related neural patterns in the prefrontal cortex
583 during sleep. *Nature Neuroscience*, 12(7), 919-926. doi:10.1038/nn.2337
- 584 37. Dragoi, G., & Tonegawa, S. (2010). Preplay of future place cell sequences by
585 hippocampal cellular assemblies. *Nature*, 469(7330), 397-401.
586 doi:10.1038/nature09633
- 587 38. Malvache, A., Reichinnek, S., Villette, V., Haimerl, C., & Cossart, R. (2016).
588 Awake hippocampal reactivations project onto orthogonal neuronal
589 assemblies. *Science*, 353(6305), 1280-1283. doi:10.1126/science.aaf3319
- 590 39. Lopes-Dos-Santos, V., Ven, G. M., Morley, A., Trouche, S., Campo-Urriza, N., &
591 Dupret, D. (2018). Parsing Hippocampal Theta Oscillations by Nested Spectral

- 592 Components during Spatial Exploration and Memory-Guided
593 Behavior. *Neuron*, 100(4). doi:10.1016/j.neuron.2018.09.031
- 594 40. Hopfield JJ (1982) Neural networks and physical systems with emergent collective
595 computational abilities. *Proc Natl Acad Sci USA* 79(8):2554–2558.
- 596 41. O, Yger P, Davison AP, Frégnac Y (2009) Reliable recall of spontaneous activity
597 patterns in cortical networks. *J Neurosci* 29(46):14596–14606.
- 598 42. Sussillo D, Abbott LF (2009). Generating coherent patterns of activity from chaotic
599 neural networks. *Neuron* 63(4):544-57.
- 600 43. Jonke Z, Legenstein R, Habenschuss S, Maass W (2017) Feedback Inhibition
601 Shapes Emergent Computational Properties of Cortical Microcircuit Motifs. *J*
602 *Neurosci* 37(35):8511–8523.
- 603 44. Fagerholm ED, Scott G, Shew WL, Song C, Leech R, Knöpfel T, Sharp DJ (2016).
604 Cortical Entropy, Mutual Information and Scale-Free Dynamics in Waking Mice.
605 *Cereb Cortex* 26(10):3945-52.
- 606 45. Prinz AA, Bucher D, Marder E (2004) Similar network activity from disparate
607 circuit parameters. *Nat Neurosci* 7(12):1345–1352.
- 608 46. Marder E, Goaillard J-M (2006) Variability, compensation and homeostasis in
609 neuron and network function. *Nat Rev Neurosci* 7(7):563–574.
- 610 47. Buzsáki G (2006) *Rhythms of the Brain* (Oxford University Press).
- 611 48. Fries P (2015) Rhythms for Cognition: Communication through Coherence. *Neuron*
612 88(1):220–235.
- 613 49. Sarasso S, et al. (2015) Consciousness and Complexity during Unresponsiveness
614 Induced by Propofol, Xenon, and Ketamine. *Curr Biol* 25(23):3099–3105.
- 615 50. Isomura, Y. et al. Integration and Segregation of Activity in Entorhinal-
616 Hippocampal Subregions by Neocortical Slow Oscillations. *Neuron* 52, 871–882
617 (2006).

- 618 51. Ferraris, M. et al. The Nucleus Reuniens Controls Long-Range Hippocampo–
619 Prefrontal Gamma Synchronization during Slow Oscillations. *The Journal of*
620 *Neuroscience* 38, 3026–3038 (2018).
- 621 52. Clement, E. A., Richard, A., Thwaites, M., Ailon, J., Peters, S., & Dickson, C. T.
622 (2008). Cyclic and Sleep-Like Spontaneous Alternations of Brain State Under
623 Urethane Anaesthesia. *PLoS ONE*, 3(4). doi:10.1371/journal.pone.0002004
- 624 53. Feldt Muldoon S, Soltesz I, Cossart R (2013) Spatially clustered neuronal
625 assemblies comprise the microstructure of synchrony in chronically epileptic
626 networks. *Proc Natl Acad Sci USA* 110(9):3567–3572.
- 627 54. Chauviere, L. et al. Early Deficits in Spatial Memory and Theta Rhythm in
628 Experimental Temporal Lobe Epilepsy. *Journal of Neuroscience* 29, 5402–5410
629 (2009).
- 630 55. Inostroza, M., Brotons-Mas, J. R., Laurent, F., Cid, E. & Prida, L. M. D. L. Specific
631 Impairment of "What-Where-When" Episodic-Like Memory in Experimental
632 Models of Temporal Lobe Epilepsy. *Journal of Neuroscience* 33, 17749–17762
633 (2013).
- 634 56. Richard, G. R. et al. Speed modulation of hippocampal theta frequency correlates
635 with spatial memory performance. *Hippocampus* 23, 1269–1279 (2013).
- 636 57. Amaral, D. & Witter, M. The three-dimensional organization of the hippocampal
637 formation: A review of anatomical data. *Neuroscience* **31**,571–591 (1989).
- 638 58. Witter, M. P., Wouterlood, F. G., Naber, P. A. & Haeflgen, T. V. Anatomical
639 Organization of the Parahippocampal-Hippocampal Network. *Annals of the New*
640 *York Academy of Sciences* **911**, 1–24 (2006).
- 641 59. Boccara, C. N. et al. A three-plane architectonic atlas of the rat hippocampal
642 region. *Hippocampus* **25**,838–857 (2015).

- 643 60. Quilichini, P., Sirota, A. & Buzsáki, G. Intrinsic Circuit Organization and Theta-
644 Gamma Oscillation Dynamics in the Entorhinal Cortex of the Rat. *Journal of*
645 *Neuroscience* 30, 11128–11142 (2010).
- 646 61. Csicsvari, J., Hirase, H., Czurkó, A., Mamiya, A. & Buzsáki, G. Oscillatory
647 Coupling of Hippocampal Pyramidal Cells and Interneurons in the Behaving
648 Rat. *The Journal of Neuroscience* 19, 274–287 (1999).
- 649 62. Harris, K. D., Henze, D. A., Csicsvari, J., Hirase, H. & Buzsáki, G. Accuracy of
650 Tetrode Spike Separation as Determined by Simultaneous Intracellular and
651 Extracellular Measurements. *Journal of Neurophysiology* 84, 401–414 (2000).
- 652 63. Hazan, L., Zugaro, M. & Buzsáki, G. Klusters, NeuroScope, NDManager: A free
653 software suite for neurophysiological data processing and visualization. *Journal of*
654 *Neuroscience Methods* 155, 207–216 (2006).
- 655 64. Fujisawa, S., Amarasingham, A., Harrison, M. T., & Buzsáki, G. (2008).
656 Behavior-dependent short-term assembly dynamics in the medial prefrontal
657 cortex. *Nature Neuroscience*, 11(7), 823-833. doi:10.1038/nn.2134
- 658 65. Adhikari, M. H., Quilichini, P. P., Roy, D., Jirsa, V. & Bernard, C. Brain State
659 Dependent Postinhibitory Rebound in Entorhinal Cortex Interneurons. *Journal of*
660 *Neuroscience* 32, 6501–6510 (2012).
- 661 66. Berens, P. (2009). CircStat: A MATLAB Toolbox for Circular Statistics. *Journal*
662 *of Statistical Software*, 31(10). doi:10.18637/jss.v031.i10
- 663 67. Hartigan, J. A., & Wong, M. A. (1979). Algorithm AS 136: A K-Means
664 Clustering Algorithm. *Applied Statistics*, 28(1), 100. doi:10.2307/2346830
- 665 68. Rousseeuw, P. J. (1987). Silhouettes: A graphical aid to the interpretation and
666 validation of cluster analysis. *Journal of Computational and Applied*
667 *Mathematics*, 20, 53-65. doi:10.1016/0377-0427(87)90125-7

- 668 69. Turing, A. M. (1937). On Computable Numbers, with an Application to the
 669 Entscheidungsproblem. Proceedings of the London Mathematical Society, S2-
 670 42(1), 230-265. doi:10.1112/plms/s2-42.1.230
 671 70. Crutchfield, J.P. (2011). Between order and chaos. *Nat Phys.* **8**, 17–24.

672

673 **Tables**

674 *Table 1 – Number of states and their oscillatory mode specificity*

675

State type	Oscillatory mode specificity	Median # states
<i>Global spectral states</i>	<i>1.0</i>	<i>2</i>
Firing substates	0.88 (0.78, 0.95)	5
Storage substates	0.80 (0.69, 0.88)	4
Sharing substates	0.86 (0.78, 0.95)	4

676 *Median (1st, 3rd quartile), all regions and conditions*

677

678 *Table 2 – Sharing assembly liquidity across regions and conditions*

679

Region and state	Liquidity sharing strengths	Liquidity sharing assemblies
mEC (<i>anesthesia</i>)	0.31 (0.22, 0.45)	0.84 (0.72, 0.89)
CA1 (<i>anesthesia</i>)	0.39 (0.36, 0.47)	0.86 (0.77, 0.89)
CA1 (<i>sleep</i>)	0.04 (0.03, 0.05)	0.57 (0.50, 0.68)
mPFC (<i>sleep</i>)	0.18 (0.11, 0.26)	0.94 (0.89, 0.96)

680 *Median (1st, 3rd quartile), SO/THE and non-REM/REM states confounded*

681

682 *Table 3 – Matching between substate sequences of different types across*
 683 *conditions and regions*

684

Type of substate matching		Relative mutual information
<i>Anesthesia (all regions confounded)</i>		
Firing substates with	Storage substates	0.38 (0.32, 0.53)
	Sharing substates	0.47 (0.36, 0.61)
Storage substates with	Sharing substates	0.38 (0.31, 0.49)
mEC substates with HPC substates (<i>all types</i>)		0.18 (0.10, 0.23)
<i>Natural sleep (all regions confounded)</i>		
Firing substates with	Storage substates	0.50 (0.46, 0.59)
	Sharing substates	0.45 (0.38, 0.66)
Storage substates with	Storage substates	0.42 (0.35, 0.57)
HPC substates with mPFC substates (<i>all types</i>)		0.42 (0.26, 0.58)

685 *Median (1st, 3rd quartile), SO/THE and non-REM/REM states confounded*

686

687 **Materials and Methods**

688 **Data information.** We use in this work a portion of the data (13 out of 18
689 experiments) initially published by Quilichini et al. (2010), which includes local field
690 potentials (LFPs) and single-unit recordings obtained from the dorsomedial entorhinal
691 cortex (mEC) of anesthetized rats. We also use a portion of the data (2 out of 16
692 experiments) initially published by Ferraris et al. (2018), which includes LFPs and
693 single-units recorded in the medial prefrontal cortex (mPFC) under anesthesia. Seven
694 recordings are original data in both mEC and dorsal hippocampus (HPC) under
695 anesthesia, and 10 recordings in 4 animals during natural sleep in HPC and mPFC. See
696 Figures S1 and S2 for details on recordings, number of cells, and layers recorded.

697 **Animal surgery.** We performed all experiments in accordance with experimental
698 guidelines approved by the Rutgers University and Aix-Marseille University Animal
699 Care and Use Committee. We performed experiments on 13 male Sprague Dawley rats
700 (250–400 g; Hilltop Laboratory Animals), 8 male Wistar Han IGS rats (250-400g;
701 Charles Rivers) and 3 male Long Evans rats (350-400g; Charles River). We performed
702 acute (anesthesia) experiments on the Sprague Dawley and 7 of the Wistar rats, which
703 were anesthetized with urethane (1.5 g/kg, i.p.) and ketamine/xylazine (20 and 2 mg/kg,
704 i.m.), additional doses of ketamine/xylazine (2 and 0.2 mg/kg) being supplemented
705 during the electrophysiological recordings. We performed chronic (natural sleep)
706 experiments on one Wistar and the Long Evans rats, which were anesthetized using
707 isoflurane 2% in 1l/min of O₂ for the surgery procedure. In both cases, the body
708 temperature was monitored and kept constant with a heating pad. The head was secured
709 in a stereotaxic frame (Kopf) and the skull was exposed and cleaned. Two miniature
710 stainless-steel screws, driven into the skull, served as ground and reference electrodes.
711 To reach the mEC, we performed one craniotomy from bregma: -7.0 mm AP and +4.0
712 mm ML; to reach the CA1 area of HPC, we performed one craniotomy from bregma: -

713 3.0 mm AP and +2.5 mm ML in the case of HPC coupled to mEC recordings, and from
714 bregma: -5.6 mm AP and +4.3 mm ML-3.0 mm in the case of HPC coupled to mPFC
715 recordings; to reach the mPFC, we performed one craniotomy from bregma: +3 mm AP
716 and +0.8 mm ML. We chose these coordinates to respect known anatomical and
717 functional connectivity in the cortico-hippocampal circuitry (51, 57-59). We used
718 different types of silicon probes to record the extracellular signals. In acute experiments,
719 the probes were mounted on a stereotaxic arm. We recorded the dorso-medial portion
720 of the mEC activity using a NeuroNexus CM32-4x8-5mm-Buzsaki32-200-177 probe
721 (in 8 experiments), a 10-mm long Acreo single-shank silicon probe with 32 sites (50
722 μm spacing) arranged linearly (in 5 experiments), or a NeuroNexus H32-10mm-50-177
723 probe (in 5 experiments), which was lowered in of the EC at 5.0-5.2 mm from the brain
724 surface with a 20° angle. We recorded HPC CA1 activity using a H32-4x8-5mm-50-
725 200-177 probe (NeuroNexus Technologies) lowered at 2.5 mm from the brain surface
726 with a 20° angle (in 4 experiments), a NeuroNexus H16-6mm-50-177 probe lowered at
727 2.5 mm from the brain surface with a 20° angle (in 2 experiments) and a E32-1shank-
728 $40\mu\text{m}$ -177 probe (Cambridge Neurotech) lowered at 2.5 mm from the brain surface
729 with a 20° angle (in 1 experiment). We recorded mPFC activity using NeuroNexus
730 H32-6mm-50-177 lowered in the layer 5 at 3 mm perpendicularly from the brain surface
731 (in 2 experiments). In chronic experiments, the probes were mounted on a movable
732 micro-drive (Cambridge Neurotech) fixed on the skull and secured in a copper-mesh
733 hat. We recorded HPC CA1 activity (probes lowered perpendicularly at 2.5 mm from
734 the brain surface) using a Neuronexus H32-Poly2-5mm-50-177 probe (in 2
735 experiments), a Cambridge Neurotech E32-2shanks- $40\mu\text{m}$ -177 probe (in 1 experiment)
736 and a NeuroNexus H32-4x8-5mm-50-200-177 probe (in 1 experiment). We recorded
737 mPFC activity (probes lowered perpendicularly at 3.0 mm from the brain surface) using
738 a NeuroNexus H32-4x8-5mm-50-200-177 probe (in 2 experiments), and a Neuronexus

739 H32-Poly2-5mm-50-177 probe (in 1 experiment). The on-line positioning of the probes
740 was assisted by: the presence of unit activity in cell body layers and the reversal of theta
741 ([3 6] Hz in anesthesia, [6 11] Hz in natural sleep) oscillations when passing from L2
742 to L1 for the mEC probe, and the presence in stratum pyramidale either of unit activity
743 and ripples (80-150 Hz) for the HPC probe, and the DV depth value and the presence
744 of intense unit activity for the mPFC.

745 At the end of the recording, the animals were injected with a lethal dose of
746 Pentobarbital Na (150mg/kg, i.p.) and perfused intracardially with 4%
747 paraformaldehyde solution. We confirmed the position of the electrodes (DiI was
748 applied on the back of the probe before insertion) histologically on Nissl-stained 40 μ m
749 section as reported previously in detail (60). We used only experiments with appropriate
750 position of the probe for analysis. The numbers of recorded single units in different
751 anatomical locations for the different retained recordings are summarized in Figure S2.
752

753 **Data collection and spike sorting.** Extracellular signal recorded from the silicon
754 probes was amplified (1000x), bandpass filtered (1 Hz to 5 kHz) and acquired
755 continuously at 20 kHz with a 64-channel DataMax System; RC Electronics or a 258-
756 channel Amplipex, or at 32 kHz with a 64-channel DigitalLynx; NeuraLynx at 16-bit
757 resolution. We preprocessed raw data using a custom-developed suite of programs (61).
758 After recording, the signals were downsampled to 1250 Hz for the local field potential
759 (LFP) analysis. Spike sorting was performed automatically, using KLUSTAKWIK
760 (<http://klustakwik.sourceforge.net> (62)), followed by manual adjustment of the clusters,
761 with the help of auto-correlogram, cross-correlogram and spike waveform similarity
762 matrix (KLUSTERS software package, <http://klusters.source-forge.net> (63)). After
763 spike sorting, we plotted the spike features of units as a function of time, and we
764 discarded the units with signs of significant drift over the period of recording.

765 Moreover, we included in the analyses only units with clear refractory periods and well-
766 defined clusters. Recording sessions were divided into brain states of theta and slow
767 oscillation periods. The epochs of stable theta (THE in anesthesia experiments, REM
768 in natural sleep experiments or slow oscillations (SO in anesthesia experiments, non-
769 REM in natural sleep experiments) periods were visually selected from the ratios of the
770 whitened power in the theta band ([3 6] Hz in anesthesia, [6 11] Hz in natural sleep)
771 and the power of the neighboring bands ([1 3] Hz and [7 14] Hz in anesthesia, [12 20]
772 Hz in natural sleep) of EC layer 3 LFP, which was a layer present in all the 18 anesthesia
773 recordings, or layer 5 mPFC recordings in natural sleep recordings, and assisted by
774 visual inspection of the raw traces (60) (Figure S3). We then used band-averaged
775 powers over the same frequency ranges of interest as features for the automated
776 extraction of spectral states via unsupervised clustering, which confirmed our manual
777 classification.

778 We determined the layer assignment of the neurons from the approximate location
779 of their somata relative to the recording sites (with the largest- amplitude unit
780 corresponding to the putative location of the soma), the known distances between the
781 recording sites, and the histological reconstruction of the recording electrode tracks.

782

783 **Characterizations of single unit activity.** We calculated pairwise cross-
784 correlograms (CCGs) between spike trains of these cells during each brain state
785 separately (60, 64-65). We determined the statistical significance of putative inhibition
786 or excitation (trough or peak in the [+2 5] ms interval, respectively) using the
787 nonparametric test and criterion used for identifying monosynaptic excitations or
788 inhibitions (60, 64-65), in which each spike of each neuron was jittered randomly and
789 independently on a uniform interval of [-5 5] ms a 1000 times to form 1000 surrogate
790 data sets and from which the global maximum and minimum bands at 99% acceptance

791 levels were constructed. Inspection of CCGs thus allowed to identify single units as
792 putatively excitatory or inhibitory, an information which we used to perform the
793 computing hub characterizations in Figure 5B.

794 To perform the analyses of Figure S4 we then computed the burst index and the
795 phase modulation of units. Burst index denotes the propensity of neurons to discharge
796 in bursts. We estimated the amplitude of the burst spike auto-correlogram (1 ms bin
797 size) by subtracting the mean value between 40 and 50 ms (baseline) from the peak
798 measured between 0 and 10 ms. Positive burst amplitudes were normalized to the peak
799 and negative amplitudes were normalized to the baseline to obtain indexes ranging from
800 -1 to 1. Neurons displaying a value of 0.6 were considered bursting.

801 To establish the phase modulation of units, we concatenated different epochs of slow
802 or theta oscillations, and estimated the instantaneous phase of the ongoing oscillation
803 by Hilbert transform of the [0.5 2] Hz or [3 6] Hz in anesthesia and [6 11] Hz in natural
804 sleep filtered signal, for slow or theta oscillations respectively. Using linear
805 interpolation, we assigned a value of phase to each action potential. We determined the
806 modulation of unit firing by Rayleigh circular statistics; $p < 0.05$ was considered
807 significant. We first assessed circular uniformity of the data with a test for symmetry
808 around the median (66) and we performed group comparison tests of circular variables
809 using circular ANOVA for uniformly distributed data and using a nonparametric multi-
810 sample test for equal medians “CM-test”, similar to a Kruskal–Wallis test, for non-
811 uniformly distributed data (Berens, 2009;
812 <https://philippberens.wordpress.com/code/circstats>), and $p < 0.05$ was considered
813 significant.

814

815 **Feature-based state extraction.** We performed a sliding-window analysis of the
816 recorded LFP time-series and single unit spike trains, extracting in a time-resolved

817 manner a variety of different descriptive features. For all the considered features (see
818 specific descriptions in later sub-sections), we use similar window sizes and overlap for
819 the sake of a better comparison. For anesthesia recordings, we adopted a long window
820 duration of 10 s – demanded by the estimation needs for the most “data-hungry”
821 information-theoretical features – with an overlap of 9 s. For natural sleep recordings,
822 we adopted a window duration of 10 s with an overlap of 9 s.

823 We computed each set of descriptive features and compiled them into multi-entry
824 vectors $\text{FeatureVector}(t)$ for every time-window centered on different times t .

825 We then compute a similarity matrix M_{sim} , to visualize the variability over time of
826 the probed feature set. The entries $M_{\text{sim}}(t_a, t_b)$ are given by the Pearson correlation
827 coefficient between the entries in the vectors $\text{FeatureVector}(t_a)$ and
828 $\text{FeatureVector}(t_b)$, treated as ordered sequences, and are thus bounded between -1
829 and +1. Blocks of internally elevated correlation along the similarity matrix diagonal
830 denote epochs of stable feature configurations. Similar configurations are detected by
831 the presence of off-diagonal highly-internally correlated blocks and the existence of
832 multiple possible configurations by the poor correlation between distinct blocks.

833 We then extracted feature-based states using a standard iterative K -means algorithm
834 (67) to cluster the different vectors $\text{FeatureVector}(t)$, based on the correlation
835 distance matrix defined by $1 - M_{\text{sim}}$. We defined the substates of different types as the
836 different clusters obtained for different feature types. We chose the number of clusters
837 K by clustering using $K = 2, 3, \dots, 20$ and first guessing K using a maximal silhouette
838 criterion (68) across all K s. We also inspected dendrograms from single-linkage
839 clustering as a cross-criterion. Using both pieces of information the K was manually
840 adjusted case-by-case (up to ± 2 clusters with respect to the unsupervised silhouette
841 criterion) to best match the visually apparent block structure of the similarity matrix
842 M_{sim} , which results in an optimized K selection for each recording.

843

844 **Feature Robustness.** To compute the robustness of the feature computation, the
845 original spiking times were randomly shuffled 1000 times and the features recomputed
846 for each instance for 2 files, one in anesthesia and one in natural sleep. To compare it
847 to the original features computed, the k for each recording and each feature was kept
848 the same. The information retained after shuffling was computed by dividing the mutual
849 information between the shuffled features and the original by the entropy of the new
850 feature set. We found a significant difference for both anesthesia and in natural sleep
851 across all features, and the results have been quantified in Table S1.

852

853 **Global oscillatory states.** We defined eight different unequally-sized frequency
854 ranges, which were manually adjusted recording-by-recording to be better centered on
855 the recording-specific positions of the slow-wave and theta peaks and of their
856 harmonics (e.g., 0–1.5 Hz, 1.5–2 Hz, 2–3 Hz, 3–5 Hz, 5–7 Hz, 7–10 Hz, 10–23 Hz and
857 23–50 Hz for the anesthesia spectrogram and the similarity matrix of Figure S3A). We
858 averaged the spectrograms over all channels within each of the layers in the
859 simultaneously recorded regions (e.g. EC and CA1 for anesthesia) and then we coarse-
860 grained the frequencies by further averaging over the eight above ranges. We compiled
861 finally all these layer-averaged and band-averaged power values into time-dependent
862 vectors $\text{Spectra}(t)$, with a number of entries given by eight (number of frequency
863 bands) times the number of layers probed in the considered recording, i.e. up to eight
864 (CA1 stratum oriens (SOr), stratum pyramidale (SP), stratum radiatum (SR) and
865 stratum lacunosum moleculare (SLM); EC layers 2, 3 and 5; and PFC layers 1,2, 3 and
866 5), yielding at most 64 entries. We then processed these spectral features as described
867 in the previous section to extract global oscillatory states –as any other substate type–
868 via unsupervised clustering.

869

870 **Firing sets and firing hubs.** Not all neurons are equally active in all temporal
871 windows. To determine typical patterns of single neuron activation we binned the
872 spiking data for each unit in 50 *ms* windows – if a neuron fired within that window the
873 result was a ‘1’, if it did not fire the result was a ‘0’. We enforced a strictly binary
874 encoding, i.e. we attributed to a bin a ‘1’ symbol even when more than one spike was
875 fired within this bin. Our bin size choice however was such to maintain the loss of
876 information when ignoring multiple firing events within a bin was less than 5%. Note
877 furthermore that for the majority of spike trains multiple firing events were extremely
878 rare, i.e. apart from a few cases the information loss was way smaller than 5%. We then
879 averaged over time this binned spike density, separately for each single unit and within
880 each time window and compiled these averages into time-dependent vectors
881 $Firing(t)$, with N entries, where N is the overall number of single units probed within
882 the considered recording. We constructed separate feature vectors for each of the
883 simultaneously recorded regions. Firing substate prototypes were given by the centroids
884 of the clusters extracted from the similarity matrix M_{sim} resulting from the stream of
885 $Firing(t)$ feature vectors.

886 We then defined a neuron to be a *high-firing cell* in a given state if its firing rate in
887 the state prototype vector was higher than the 95% percentile of all concatenated state
888 prototype vector entries.

889

890 **Active Information Storage.** Within each time-window we computed for each
891 single unit an approximation to the Active Information Storage (AIS). AIS is meant to
892 quantify how much the activity of a unit is maintaining over time information that it
893 was conveying already in the past (3, 6). This information-theoretical notion of storage
894 is distinct from the neurobiological notion of storage in synaptic weights. It is indeed

895 an activity-based metric (hence the adjective “active”), able to detect when temporal
896 patterns in the activity of a single unit can serve the functional role of “memory buffer”.

897 AIS is strictly defined as:

898

$$899 \quad \text{AIS}_i = \text{MI}[i(t), i(\rightarrow t)]$$

900

901 i.e. as shared information between the present activity $i(t)$ of a single unit i and its past
902 history of activity $i(\rightarrow t)$ (cf. Figure S6A). Prior to computing mutual information, we
903 binned all spike trains with method as for determining the $\text{Firing}(t)$ descriptive
904 feature vector. The limited amount of available data within each temporal window
905 makes necessary to introduce approximations. Therefore, we replaced the full past
906 history of activity $i(\rightarrow t)$ with activity at a time in the past $i(t-\tau)$ and then summed over
907 all the possible lags:

908

$$909 \quad \hat{\text{AIS}}_i = \sum_{\tau} \text{MI}[i(t), i(t-\tau)]$$

910

911 where the lag τ was varying in the range $0 \leq \tau \leq 0.5T_{\theta}$, where T_{θ} is the phase of the theta
912 cycle. Note that MI values were generally vanishing for longer latencies (cf. Figure
913 S13A). We evaluated MI terms using a ‘plug-in’ function estimator on binarized spike-
914 trains, which takes the binned spike trains of two neurons for a defined time window
915 and computes the mutual information and entropy values of the two variables (6).
916 Concretely speaking, we estimated the probability p that a bin includes a spike and the
917 complementary probability $1 - p$ that a bin is silent for each unit, by direct counting of
918 the frequency of occurrence of “1”s and “0”s in the binned spike trains of each unit.
919 These counts yielded the probability distributions $P(i)$ and $P(j)$ that two neurons i and j
920 fire or not. Analogously, we sampled directly from data the histogram $P(i,j)$ of joint

921 spike counts for any pair of two units i and j . These histograms were then directly
922 “plugged in” (hence the name of the used estimator) into the definition of MI itself:

$$923 \quad MI(i, j) = \sum_i \sum_j P(i, j) \log_2 \frac{P(i, j)}{P(i)P(j)}$$

924 We then subtracted from each MI value a significance threshold (95-th percentile of
925 MI estimated on shuffled binarized trains, 1000 replicas), putting to zero non-
926 significant terms (and thus negative after bias subtraction). Although such corrected
927 plug-in estimator is very rough, it is sufficient in our application in which we are not
928 interested in quantitatively exact values of MI but just in relative comparisons of values,
929 finalized to state clustering over a large amount of observations. We compiled the N
930 resulting $\hat{A}IS_i$ values into time-dependent vectors $Storage(t)$, constructing separate
931 vectors for each of the simultaneously recorded regions. We then constructed storage
932 substates through unsupervised clustering based on the M_{sim} matrices, as previously
933 described. We defined a neuron to be a *storage hub* in a given state if its $\hat{A}IS_i$ value in
934 the state prototype vector was higher than the 95% percentile over all entries of
935 concatenated cluster prototype vectors. Such conservative threshold guarantees that
936 only neurons with exceptionally high AIS values are labeled as hubs. While we may
937 have some false negatives –i.e. neurons with values in the right tail of the AIS
938 distribution not labeled as hubs–, we are thus protected against false positives.

939 AIS absolute values varied widely between the different recordings. To compare AIS
940 measures and their relative changes between global oscillatory states across recordings,
941 we first averaged AIS for all the units within a specific anatomic layer. We then
942 normalized these average AIS values by dividing them by the average AIS value in the
943 SO state (in anesthesia) or the nonREM state (in natural sleep) for the specifically
944 considered recording and layer. The results of this analysis are shown in Figure S7,
945 where different lines correspond to different recordings.

946

947 **Information sharing networks and strengths.** Within each time-window we
948 computed time-lagged Mutual Information $MI[i(t), j(t-\tau)]$ between all pairs of spike
949 density time-series for different single units i and j (evaluated via the same binning
950 method for determining the $Firing(t)$ descriptive feature vector). Although MI is not
951 a directed measure, a pseudo-direction of sharing is introduced by the positive time-lag,
952 supposing that information cannot be causally shared from the future. Thus, for every
953 directed pair of single units i and j (including auto-interactions, with $i = j$), we defined
954 pseudo-directed information sharing as:

955

$$956 \quad I_{shared}(j \rightarrow i) = \sum_{\tau} MI[i(t), j(t-\tau)]$$

957

958 where the lag τ was varying in the range $0 \leq \tau \leq 0.5T_{\theta}$, where T_{θ} is the phase of the
959 theta cycle. Once again, we estimated MI terms via direct plug-in estimators on
960 binarized spike trains, as with storage, subtracting a significance threshold (95-th
961 percentile of MI estimated on shuffled binarized trains, 400 replicas) and zeroing not
962 significant terms. All these $I_{shared}(j \rightarrow i)$ entries were interpreted as weights in the
963 adjacency matrix of an information sharing directed functional network, and we defined
964 as *sharing assembly* formed by a neuron i the star-subgraph of the information sharing
965 network composed of i and all its immediate neighbors. We compiled all the overall N^2
966 different values of $I_{shared}(j \rightarrow i)$ into time-dependent feature vectors $Sharing_A(t)$,
967 describing thus all the possible sharing assemblies at a given time. We then also
968 computed *information sharing strengths* by integrating the total amounts of information
969 that each single unit was sharing with the past activity of other units in the network
970 (“sharing-in”):

971

972
$$I_{shared}(\rightarrow i) = \sum_j I_{shared}(j \rightarrow i)$$

973

974 or with the future activity of other units in the network (“sharing-out”):

975

976
$$I_{shared}(i \rightarrow) = \sum_j I_{shared}(i \rightarrow j)$$

977

978 In other words, the integrated amount of shared information was given by the in-
979 strength and the out-strength of a node in the information sharing network with
980 individual link weights $I_{shared}(j \rightarrow i)$. We compiled the N incoming $I_{shared}(\rightarrow i)$ and N
981 outgoing $I_{shared}(i \rightarrow)$ values into time-dependent vectors $Sharing_S(t)$. We computed
982 separate $Sharing_A(t)$ and $Sharing_S(t)$ for each of the simultaneously recorded
983 regions. We then performed as before unsupervised clustering based on the associated
984 M_{sim} matrices to extract sharing substates. Since the block structure displayed by the
985 M_{sim} matrices for sharing assemblies and strengths are nearly perfectly overlapping we
986 conducted all substate analyses based on $Sharing_S(t)$ vectors only. We defined a
987 neuron to be a *sharing hub* in a given state if its $I_{shared}(* \rightarrow i)$ and/or $I_{shared}(i \rightarrow *)$ values
988 in the state prototype vector were higher than the 95% percentile of all concatenated
989 cluster prototypes entries (again protecting against false positive detection).

990 The relative comparisons of information sharing between SO and THE (REM and
991 nonREM) epochs for different recordings shown in Figure S9, are based, as in the case
992 of AIS in Figure S7, on averaged and scaled values. We first averaged the total I_{shared}
993 (i.e. sharing in plus sharing out) over all the units within a specific anatomic layer. We
994 then normalized these average total I_{shared} values by dividing them by the average total
995 I_{shared} value in the SO state (in anesthesia) or the nonREM state (in natural sleep) for
996 the specifically considered recording and layer.

997 **Liquidity of sharing.** The M_{rec} matrices for Sharing Assemblies display light blue
998 (low internal correlation) blocks while the M_{rec} matrices for Sharing Strengths have
999 similar blocks but red-hued (higher internal correlation). We quantify this visual
1000 impression by evaluating liquidity of sharing strength and sharing assembly substates.
1001 For a given recording and a given associated M_{rec} matrix (e.g. the one for the
1002 `Sharing_A` or the `Sharing_S` features), we define T_α as the set of times t for which
1003 the system is in a given substate α relative to the considered feature of interest. We then
1004 evaluate the liquidity $\Lambda(\alpha)$ of this substate α as:

$$1005 \quad \Lambda(\alpha) = \frac{\sum_t \sum_{t' < t}^{t \in T_\alpha, t' \in T_\alpha} (1 - |M_{rec}(t, t')|)}{\binom{\#T_\alpha}{2}}$$

1006 where $|\cdot|$ denotes the absolute value operator and $\#T_\alpha$ is the number of elements of the
1007 set T_α . Liquidity values are thus bounded in the interval $0 \leq \Lambda(\alpha) \leq 1$, with 1 indicating
1008 maximum liquidity (i.e. maximum internal variability) of a substate.

1009

1010 **Oscillatory mode specificity and hub distributions.** For each substate (firing,
1011 storage, sharing) we computed the fraction of times that the substate was observed
1012 during a SO or a THE state (in anesthesia) or a nonREM or REM state (in natural sleep).
1013 We defined the largest among these fractions as the oscillatory specificity of this
1014 substate. Oscillatory specificities close to 1 indicate that a substate occurs mostly within
1015 one of the two possible global states observed in each recording, while specificities
1016 close to 0.5 indicate that the substate do not occur preferentially in one of the global
1017 states.

1018 To evaluate the probability that a hub emerges in a given anatomical layer, we
1019 computed for every recording the fraction of cells recorded in each layer that were
1020 labeled as hubs at least in one computing substate (storage or sharing). We computed
1021 separately these fractions layer-by-layer, for excitatory and inhibitory cells and for

1022 anesthesia or sleep. These fractions were equal to unit when all the excitatory (or
1023 inhibitory) cells in a layer happened to be hubs at least once. We then evaluated the
1024 general probability that a hub emerges in a layer, which is different from the previous
1025 one, because it takes in account as well the fact that some cells may be labeled as hubs
1026 more often than others. We then considered the list of all hubs of a given type (storage
1027 or sharing) across all substates, including repetitions (if a neuron was hub in more than
1028 one substate then it appeared multiple times in the list) and evaluated the fraction of
1029 times in which a hub in this list was belonging to a given layer. We computed separately
1030 these fractions layer-by-layer, for storage or sharing hubs and for anesthesia or sleep.
1031 95% confidence intervals for the mean fractions above were evaluated as 2.996 times
1032 their sample standard deviation over the different recordings for which they could be
1033 computed. We considered two mean fractions to be different when their 95%
1034 confidence intervals were fully disjoint.

1035

1036 **Coordination between substate transitions.** To compare sequences of substates
1037 of different types or in different regions we introduced a symbolic description of
1038 substate switching. Each substate was assigned a *letter* symbol, i.e. a label $s^{(p)}$ where p
1039 can stand for firing, information storage or sharing and $s^{(p)}$ is an arbitrary integer label
1040 different for every substate. We could thus describe the temporal sequences of the
1041 visited substates of each different type as an ordered list of integers $s^{(p)}(t)$. We quantified
1042 the degree of coordination between the sequences of substates of different types (e.g. p
1043 = ‘storage’ vs q = ‘sharing’) or in different regions (e.g. p = ‘storage in EC’ vs q =
1044 ‘storage in CA1’) by evaluating the relative Mutual Information term:

1045

1046
$$\text{MI}[s^{(p)}(t), s^{(q)}(t)] / \max[\text{H}(s^{(p)}(t)), \text{H}(s^{(q)}(t))]$$

1047

1048 normalized between 0 –full statistical independence between the two substate
1049 sequences– and 1 –complete overlap between the two substate sequences–, by dividing
1050 it by the entropy H of the most entropic among the two symbolic streams. We evaluated
1051 these MI and H terms using direct plug-in estimators on the joint histograms of substate
1052 labels. We estimated chance expectations for the level of coordination by repeating the
1053 same procedure for substate sequences with shuffled substate labels and then finding
1054 the 99th percentile over 1000 permutation replicas of the computed MI/ H .

1055

1056 **Mutual Information Measure’s Dependence on Bin Size.** The original decision
1057 for the bin size was chosen such that when discretized, the information content lost by
1058 counting 2 or 3 spikes on the same neuron within a given bin as a ‘1’ was less than 5%.
1059 On average, the information content lost was less than 1% across all recordings. To
1060 analyze the dependence on bin sizes, one example recording was chosen in the PFC
1061 during natural sleep in different bin sizes, 25 *ms*, 33 *ms* and 66 *ms* and computed
1062 substates using the same methods described above. To make the comparison focused
1063 on bin size, the same number of clusters per feature was chosen to reflect the original
1064 number. We then computed the amount of information about the substate sequences
1065 computed with the original binsize were retained by corresponding substate sequences
1066 derived for each different bin size. To do so, we used the same procedure described in
1067 the previous section to quantify coordination between sequences for different types of
1068 states or between different regions. Notably we computed mutual information between
1069 the substate sequences for different bin-sizes (normalized by the entropy of the original
1070 sequence) and compared this relative mutual information with chance expectation
1071 (obtained via shuffling substate sequences, as above). We found that the mutual
1072 information between corresponding sequences for different bin sizes was two order of
1073 magnitudes above chance level (Figure S13B), denoting high robustness of our

1074 procedure for extracting substates. Correspondingly, we also found that, for matched
1075 substates between sequences extracted for different bin-sizes, the identification, number
1076 and anatomical localization of hubs were only marginally altered.

1077 **Complexity of substate sequences.** After converting sequences of substates into
1078 symbolic streams of letters, we defined substate *words* as the triplets of letters
1079 corresponding to the firing, the information storage and the information sharing
1080 substates simultaneously observed at each time t , i.e.:

1081

$$1082 \quad S(t) = s^{(firing)}(t) s^{(storage)}(t) \dots s^{(sharing)}(t)$$

1083

1084 We then constructed a *switching table* T in which the temporally ordered columns
1085 provide the sequence of substate words $S(t)$ along time. We compiled separate
1086 switching tables for each recording and for each of the simultaneously recorded regions.
1087 The total set of substate words effectively found in a specific switching table constitutes
1088 its associated *dictionary* of substate combinations. We defined then the *used dictionary*
1089 *fraction*, as the ratio between the number of observed words and the maximum
1090 theoretically possible number of words that could have been composed given the
1091 available substate letters (depending on how many firing, storage or sharing substates
1092 have been effectively extracted).

1093 We then evaluated the complexity of substate word sequences using a procedure
1094 inspired from the notion of Kolmogorov-Chaitin complexity (19) and minimum
1095 description length approaches (MDL; 20). The basic concept is that, for a regular
1096 symbolic sequence (as our streams of substate words), it will be possible to design a
1097 tailored “compression language” such the sequence will admit a much shorter
1098 description when reformulated into this language with respect to the original length in
1099 terms of number of words. On the contrary, a random symbolic sequence will be poorly

1100 compressible, i.e. its descriptions in terms of a generative language will be nearly as
1101 long as the original list of symbols appearing in the sequence. A complex symbolic
1102 sequence will stand between these two extremes - still admitting a compressed
1103 generative description but not as short as for regular sequences. Departing from
1104 universal compression approaches, as the original MDL formulation (20) or the
1105 Lempel-Ziv approach (21), we introduce here a “toy language” for generative
1106 description, specialized to compress state transition tables as the ones of Figure 6A. Our
1107 choice is conceptually compliant with the MDL approach but – for the sake of
1108 pedagogy– avoids technical steps as the use of binary prefix coding.

1109 Let $\Omega = \{S_1, S_2, \dots, S_\omega\}$ be the dictionary of substate words appearing in the switching
1110 table T which we want to describe. We first define the *exhaustive list description* (D_{list})
1111 of T as a string of the following form:

1112

$$1113 \quad D_{\text{list}} := S_1 t_{1,1} t_{1,2} \dots t_{1,k_1} S_2 t_{2,1} t_{2,2} \dots t_{2,k_2} \dots S_\omega t_{\omega,1} t_{\omega,2} \dots t_{\omega,k_\omega}$$

1114

1115 In such a description the symbol of each substate word S_q (counting as one description
1116 unit) is followed by an exhaustive list of all the k_q times $t_{q,1}, t_{q,2}, \dots, t_{q,k_q}$ (each time
1117 index counting as an extra description unit) at which the recorded system produced the
1118 matching substate word. If the number of analyzed time windows is $K = k_1 + k_2 + \dots +$
1119 k_ω , then the length of the exhaustive list description will be $|D_{\text{list}}| = K + \omega$ description
1120 units (K time stamps, plus ω substate word symbols).

1121 Let then define the *block-length description* (D_{block}) of the stream of substate
1122 codewords, as a description of the following form:

1123

$$1124 \quad D_{\text{block}} := S_1 w_{1,1} l_{1,1} w_{1,2} l_{1,2} \dots w_{1,m_1} l_{1,m_1} S_2 w_{2,1} l_{2,1} w_{2,2} l_{2,2} \dots w_{2,m_2} l_{2,m_2} \dots$$

1125 $S_{\omega} w_{\omega,1} l_{\omega,1} w_{\omega,2} l_{\omega,2} \dots w_{\omega,m\omega} l_{\omega,m\omega}$

1126

1127 In such a description the symbol of each word S_q (always counting as one description
1128 unit) is followed by a list of stepping instructions for a hypothetical “writing head”
1129 moving along different discrete positions on an idealized tape, similarly to computing
1130 automata as the Turing Machine (69). At the beginning the machine is initialized with
1131 the head on the first position on the tape. The integers $w_{q,n}$ –at odd positions (1st, 3rd,
1132 etc.) after the word symbol– indicate for how many steps the machine head must shift
1133 on the tape toward the right *without* writing, but just skipping positions. The integers
1134 $l_{q,n}$ –at even positions (2nd, 4th, etc.) after the word symbol– indicate instead for how
1135 many steps the machine must also write on the tape the symbolic string S_q before then
1136 shifting to the next position on the right. Every time that a new symbol S_q is met when
1137 parsing the step lengths description, the position of the writing head is reset to the
1138 leftmost starting position on the tape. Such parsing grammar is obviously more complex
1139 than the one for a simpler “parrot machine”, designed to parse exhaustive list
1140 descriptions as the ones described above. The length in symbols of this block-length
1141 description is variable and depends on how regular the word sequence is to compress
1142 and regenerate. The block-length description segment $S_q w_{q,1} l_{q,1} \dots w_{q,mq} l_{q,mq}$ will be
1143 shorter than the matching exhaustive list description segment $S_q t_{q,1} \dots t_{q,kq}$ whenever
1144 $2m_p < k_p$, which can happen if transitions for the different types of substate letters are
1145 regularly aligned, in such a way that the resulting switching table have long alternating
1146 blocks with repeated substate words.

1147 The syntactic complexity of a sequence of substate words can then be evaluated by
1148 quantifying how much the program to generate the switching table T via a “smart”
1149 compressing machine interpreting block-length descriptions is shorter than the program

1150 to generate the same table T via a “dumb” parrot machine interpreting exhaustive length
1151 descriptions. We define the *description length complexity* of a switching table T as:

1152

$$1153 \quad \text{DLC} = |D_{\text{block}}(T)| / |D_{\text{list}}(T)|$$

1154

1155 To give a toy example, let’s consider the sequence $T = \text{“AAAAAAA BBBB AAAAA}$
1156 $\text{CCCCC DDD BBBB} \text{”}$, built out of four possible collection of substate words $S_1 =$
1157 A , $S_2 = B$, $S_3 = C$ and $S_4 = D$. The exhaustive list description for this sequence will be:

1158

$$1159 \quad D_{\text{list}}(T) = A \ 1 \ 2 \ 3 \ 4 \ 5 \ 6 \ 7 \ 12 \ 13 \ 14 \ 15 \ 16 \ B \ 8 \ 9 \ 10 \ 11 \ 25 \ 26 \ 27 \ 28 \ 29 \ 30$$
$$1160 \quad \quad \quad C \ 17 \ 18 \ 19 \ 20 \ 21 \ D \ 22 \ 23 \ 24$$

1161

1162 with length $|D_{\text{list}}(T)| = 34$ descriptive units. Its step lengths description will be:

1163

$$1164 \quad D_{\text{block}}(T) = A \ 0 \ 7 \ 4 \ 5 \ B \ 7 \ 4 \ 13 \ 6 \ C \ 16 \ 5 \ D \ 21 \ 3$$

1165

1166 with length $|D_{\text{block}}(T)| = 16$ descriptive units, i.e. $|D_{\text{block}}(T)| < |D_{\text{list}}(T)|$.

1167 Given the noisiness of data, we dropped from both the exhaustive list description
1168 and the step lengths description the segments corresponding to exceedingly rare words
1169 S_q . In particular, ranking the code words from the least to the rarest, we dropped all the
1170 words S_r with $r \geq R$, such that removing all of their occurrences in the word stream
1171 reduced the stream’s overall length of no more than 10% (lossy compression).

1172 We computed confidence intervals for DLC values via a Jackknife construction in
1173 which we drop one word at random position from the temporal stream $S(t)$ made of K
1174 symbols, generating up to K Jackknife surrogate streams, each with $K-1$ symbols. The

1175 confidence interval was then given by the 5-th and the 95-th percentile over the
1176 complexities evaluated from these Jackknife surrogates.

1177 Appropriate reference criteria were then required to discriminate complex vs ordered
1178 or random switching tables. We need to compare the empirically observed DLC values
1179 against two thresholds. Complex switching tables should have indeed a DLC below a
1180 threshold for randomness testing and above a threshold for regularity testing. Given a
1181 switching table T , we constructed a randomized version T_{rand} by randomly permuting
1182 independently the entries of each of its rows. For each recording, we constructed 1000
1183 instances of T_{rand} and evaluated DLC for all of them, identifying as upper threshold for
1184 complexity the 5-th percentile $\text{DLC}_{\text{rand}} = q_{5\%}[\text{DLC}(T_{\text{rand}})]$. We then constructed an
1185 enhanced-regularity version T_{regular} of each T by lexicographically sorting entries row-
1186 by-row (to get blocks of homogeneous code-words as long-lasting as possible based on
1187 exactly the same building bricks). We then arbitrarily defined a lower threshold for
1188 complexity $\text{DLC}_{\text{regular}} = 2 \text{DLC}(T_{\text{regular}})$. The thresholds $\text{DLC}_{\text{regular}}$ and DLC_{rand} varied for
1189 every switching table. However, the criterion $\text{DLC}_{\text{regular}} < \text{DLC} < \text{DLC}_{\text{rand}}$ was fulfilled
1190 for all the considered recordings, whose state transitions sequences could then be
1191 certified to be complex (in our arbitrary but quantitative and operational sense).

1192 Importantly, we could restrict the evaluation of complexity to sub-table restricted to
1193 words occurring during selected different global oscillatory states only. In this way we
1194 could compare the complexity of sequences occurring within different global states,
1195 e.g. REM vs nonREM. We plot in Figure 6E relative complexity variations between
1196 two global states α and β :

1197

$$1198 \quad \Delta(\text{DLC}) = (\text{DLC}_{\alpha} - \text{DLC}_{\beta}) / (\text{DLC}_{\alpha} + \text{DLC}_{\beta})$$

1199

1200 We evaluated once again confidence intervals for relative complexity variations via
1201 one-leave-out Jackknife on global state-restricted switching table columns.

1202

1203 **Burstiness of state sequences.** We also characterize switching tables in terms of
1204 their “style” of transitions, looking at two different temporal statistics. First, we
1205 computed all *inter-transition times* from a table \mathcal{T} , i.e. the number of time-steps
1206 occurring between one block (continuous time-interval with a same substate word
1207 maintained in time) to the next. Note that these inter-transition times are precisely the
1208 $l_{p,n}$ integers appearing in the block-length description $D_{\text{block}}(\mathcal{T})$ of the table \mathcal{T} . After
1209 computing the mean μ_l and the standard deviation σ_l of these inter-transition times, we
1210 then evaluated the burstiness coefficient (22):

1211

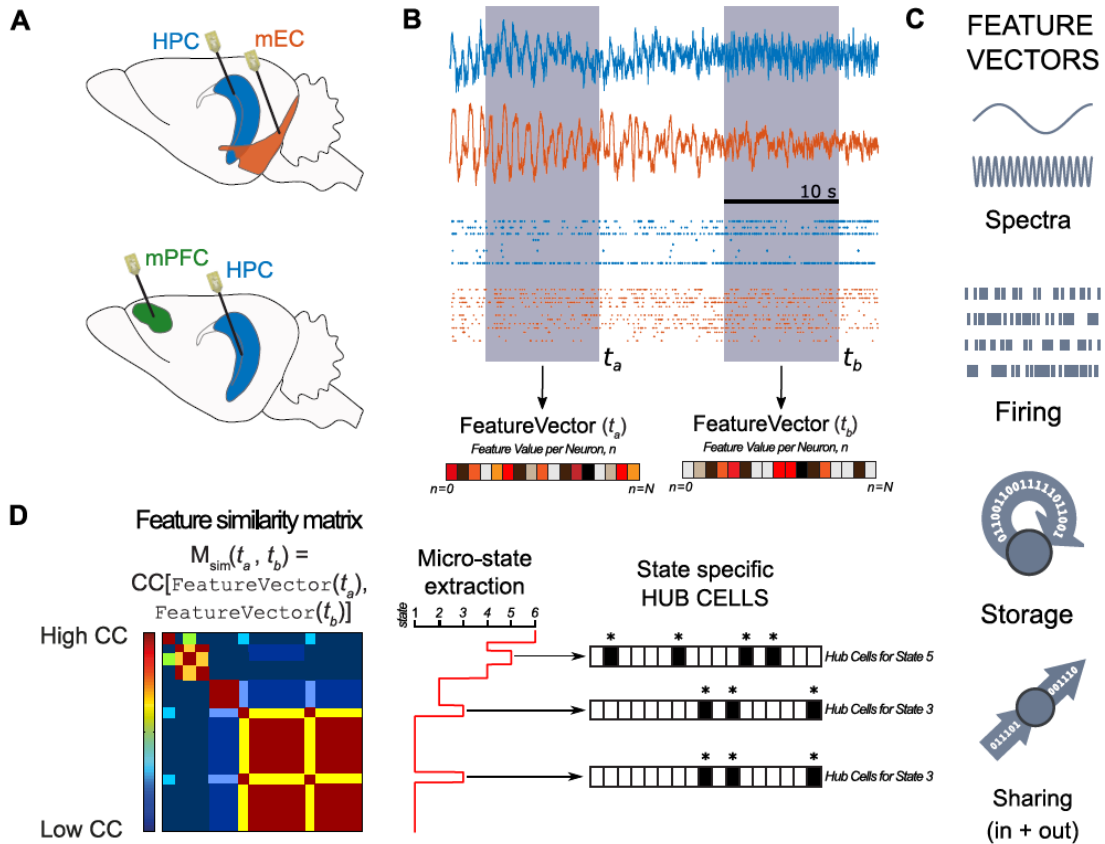
1212
1213

$$B = \frac{\frac{\sigma_l}{\mu_l} - 1}{\frac{\sigma_l}{\mu_l} + 1}$$

1214 Such a coefficient is bound between $-1 < B < 1$ and is equal to 0 when transitions
1215 between substate words follow a Poisson statistic, negative when the train of transitions
1216 is more periodic and positive when more bursty than for a Poisson train.

1217

1218 **Figures**



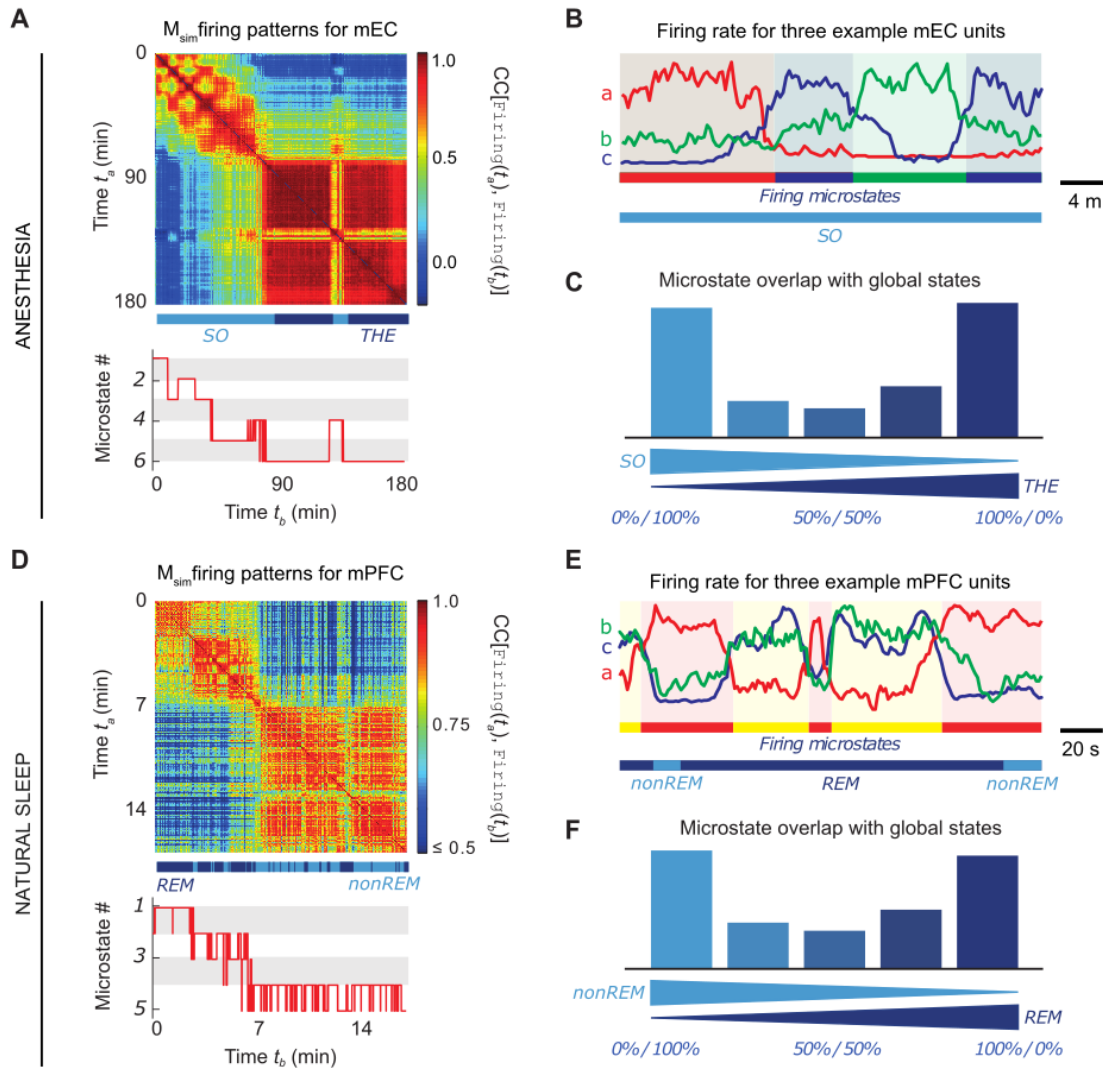
1219

1220

1221 **Figure 1. Unsupervised extraction of states and hubs.** **A.** Cartoon representing the
 1222 approximate recording locations (mEC and CA1, mPFC and CA1) during 2 experiment
 1223 types in anesthesia and sleep. **B.** Example LFP trace taken from the 32 channels in
 1224 CA1 (blue) and 32 channels in mEC (orange). Below are examples of isolated unit
 1225 activity taken from the same recording. For each time window (t), we extract different
 1226 features represented by the $FeatureVector(t)$, which has a feature value for each
 1227 channel or single unit recorded. **C.** We consider four features: spectral band averaged
 1228 powers (from LFP channels); single unit firing rates; information storage and
 1229 information sharing. **D.** Left panel: A cartoon representation of M_{sim} . To extract
 1230 substates and their temporal dynamics, we construct a *feature similarity* matrix M_{sim} in
 1231 which the entry $M_{sim}(t_a, t_b)$ measures Pearson correlation between the vectors

1232 FeatureVector(t_a) and FeatureVector(t_b). Time flows from the top-left corner
1233 horizontally to the top-right corner and vertically to the bottom-left corner. A block
1234 (square) along the diagonal in the resulting image identifies a period of feature stability,
1235 i.e. a substate. A block appearing several times horizontally or vertically indicates that
1236 a feature is repeated several times. Middle panel: Unsupervised clustering identifies the
1237 different substates (indicated by a number) and their temporal dynamics (the vertical
1238 axis corresponds to that of the similarity matrix). Right panel: We identify computing
1239 hub cells, i.e. neurons that display exceptionally high values for a given feature,
1240 associated with given substates. Note that reoccurring states have the same hub cells
1241 (state 3 in this example).

1242



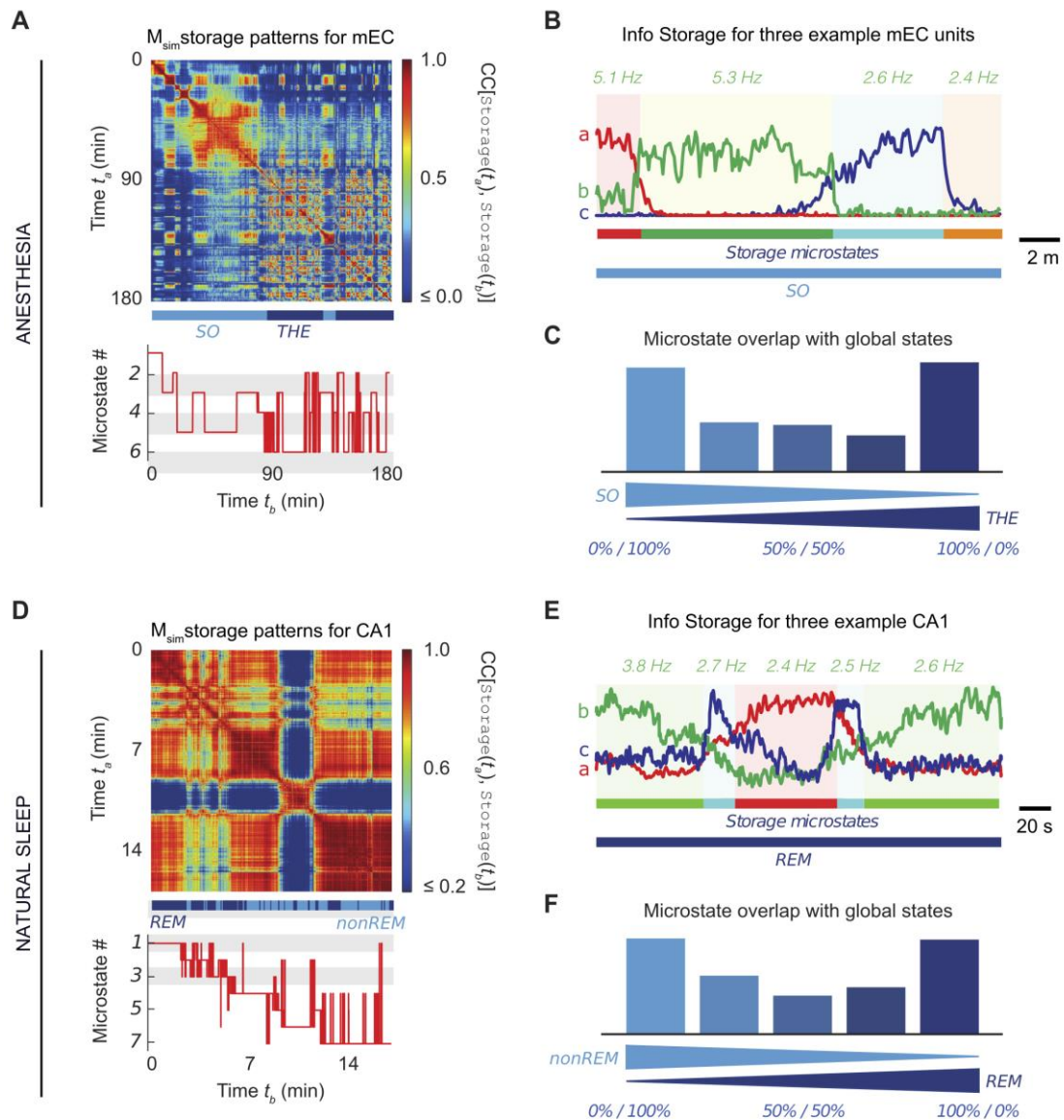
1243

1244

1245 **Figure 2. Firing substates.** Examples of similarity matrices M_{sim} obtained from
 1246 $Firing(t)$ at different times in mEC during anesthesia (**A**) and in mPFC during natural
 1247 sleep (**D**), measured in two animals. The bar below M_{sim} indicates the transitions
 1248 occurring between THE/REM (dark blue) and SO/nonREM (light blue). Although there
 1249 were only two global brain states, six (**A**) and five (**D**) firing substates were identified.
 1250 Panels (**B**) and (**E**) show examples of the firing density of three neurons (a, b and c)
 1251 recorded in mEC and mPFC, respectively, with amplitude normalized for visualization.
 1252 Neurons tended to fire in specific substates, indicated here with a color code. These
 1253 examples also illustrate the switching between different firing substates inside a given

1254 global oscillatory state, and their overlap across different global oscillatory states. The
1255 analysis of all recordings revealed that a majority of firing substates tended to occur
1256 during a preferred global oscillatory state, as indicated by the bimodal histograms
1257 during anesthesia (**C**) and natural sleep (**F**), respectively.

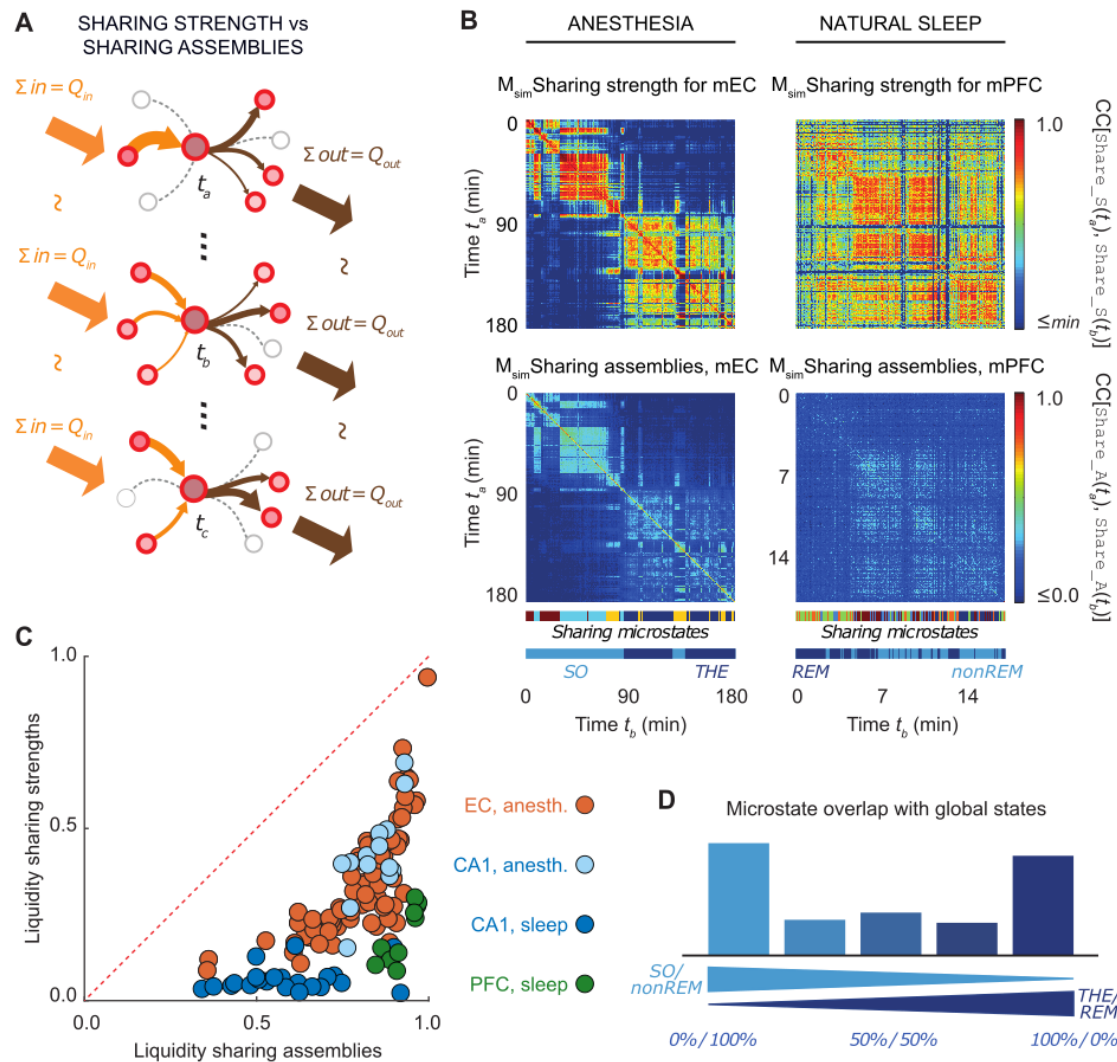
1258



1259

1260 **Figure 3. Information storage substates.** Examples of similarity matrices M_{sim}
 1261 obtained from $Storage(t)$ at different times in mEC during anesthesia (**A**) and CA1
 1262 during natural sleep (**D**). As for firing substates, we identified more storage substates
 1263 (6 and 7, respectively, in the shown examples) than global oscillatory states. We show
 1264 in panels (**B**) and (**E**) that the participation of three individual neurons to information
 1265 storage (indicated in arbitrary units for visualization) was substate-dependent. The
 1266 values reported above the plots correspond to the average firing rate of the neuron b
 1267 (green color) during the corresponding epochs within consistent storage substates. The
 1268 analysis of all recordings showed that storage substates tended to occur during a

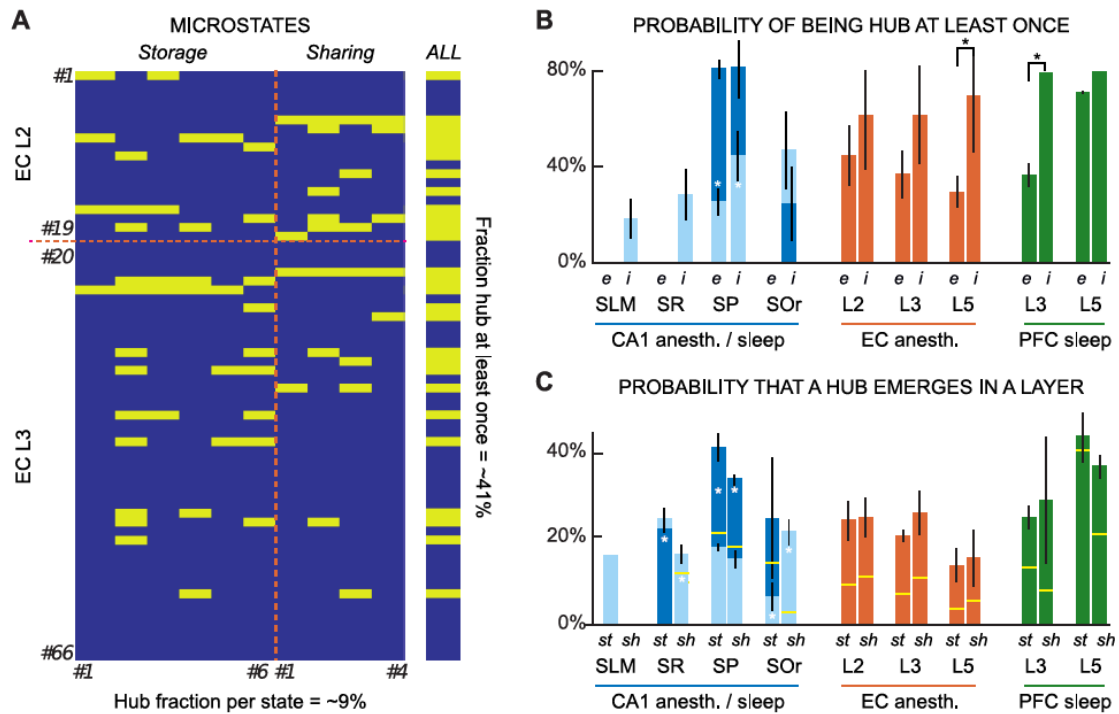
1269 preferred global oscillatory substate, as indicated by the bimodal histograms for
 1270 anesthesia (C) and for natural sleep (F).
 1271



1272

1273 **Figure 4. Information sharing substates.** The cartoon in panel A shows an example
 1274 of sharing assembly for a given sharing hub neuron across 3, non-sequential
 1275 occurrences of the same substate. The total strength of in- and out-going sharing is equal
 1276 (large, external arrows) during t_a , t_b , and t_c while the assembly changes (smaller, internal
 1277 arrows). The changing size of internal arrows represent the sharing strength of that
 1278 particular functional connection between the sharing hub and its source and target

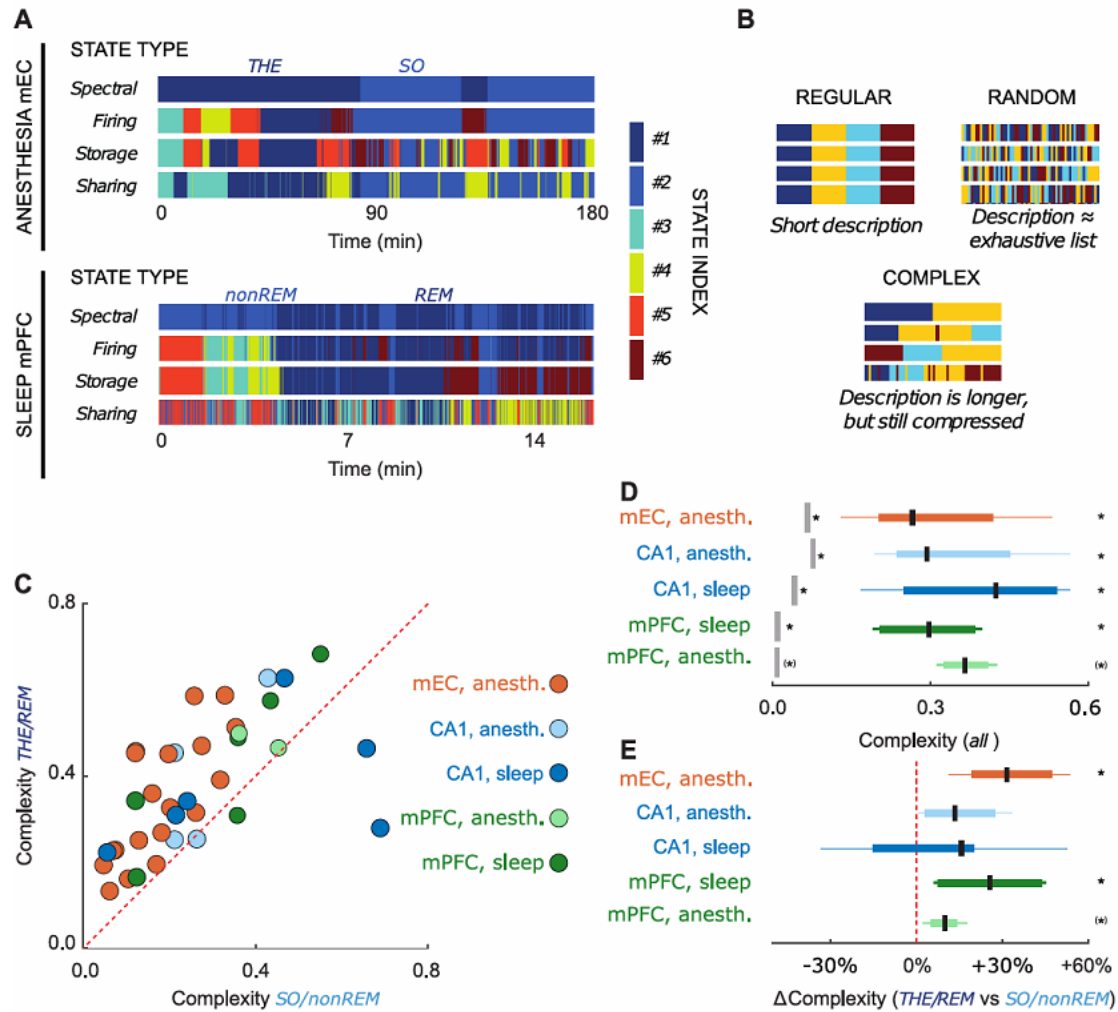
1279 neurons. **(B)** Similarity matrices M_{sim} for sharing strengths $Sharing_S(t)$ (top) and
1280 sharing assemblies $Sharing_A(t)$ (bottom), in mEC during anesthesia (left) and
1281 mPFC during natural sleep (right). We identified a multiplicity of substates within each
1282 global oscillatory state as shown by the colored bars below the feature similarity
1283 matrices. The similarity matrices for sharing strengths and assemblies have a matching
1284 block structure. However, sharing strengths were very stable within a substate (red-
1285 hued blocks), while sharing assemblies were highly volatile (light blue-hued blocks).
1286 This is quantified for each sharing assembly substate by a *liquidity* coefficient **(C)**. As
1287 shown in **(C)**, for all observed sharing substates across all regions and global oscillatory
1288 states in all animals, the liquidity of sharing assemblies was much larger than the one
1289 of sharing strengths. Finally, **(D)** demonstrates that most sharing substates occurred
1290 preferentially during a preferred global oscillatory state for both anesthesia and natural
1291 sleep combined (see Figure S7 for separated histograms for the two conditions).
1292



1293

1294 **Figure 5. A democracy of computing hubs.** (A) Within every computing substate
 1295 some neurons exhibited significantly strong values of information storage or sharing
 1296 (*computing hubs*). However, these computing hubs did generally change from one
 1297 substate to the other, as shown in this example. Different rows correspond to different
 1298 single units recorded in mEC during anesthesia and different columns correspond to
 1299 different computing substates (left, storage substates 1 to 6; right, sharing substates 1
 1300 to 4). An entry is colored in yellow when the neuron is a computing hub within the
 1301 corresponding substate. In the shown example, while ~9% of neurons on average were
 1302 simultaneously acting as computing hub, over 40% of the recorded units were recruited
 1303 as hubs for at least one substate, when considering all the computing substates together
 1304 (vertical bar on the right). (B-C) The probability that a neuron acted as hub depended
 1305 only loosely on its anatomical localization. Panel B shows that for all regions and layers
 1306 the probability that a neuron act as computing hub at least once was always larger than
 1307 30%. Inhibitory (*i*) neurons tended to be recruited as hubs more frequently than
 1308 excitatory (*e*) neurons. Analogously, panel C shows that none of the layers display a

1309 specialization in either one of the two processing operations of information storage or
1310 sharing. Stars denote statistically significant comparisons (lack of overlap between 95%
1311 confidence intervals for the probability, reported as vertical ranges on top of the
1312 histogram bar). In panel **C** a yellow horizontal line indicates the fraction of computing
1313 hub cells which also happen to simultaneously be high-firing rate cells. Many
1314 computing hubs have thus average or low firing rate. In panel **B-C** in CA1 light blue
1315 represents anesthesia and dark blue represents natural sleep.

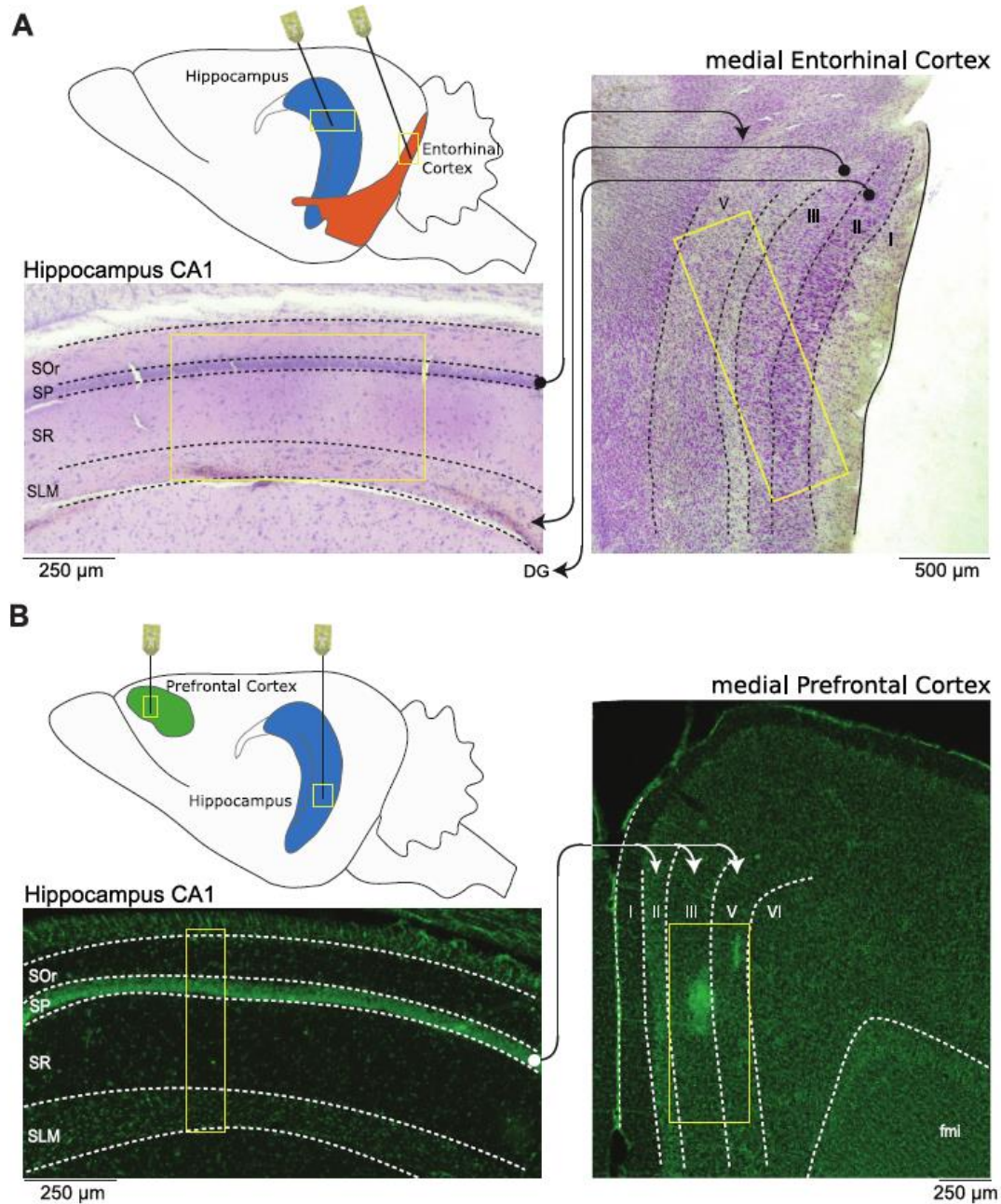


1316

1317 **Figure 6. Complexity of substate sequences.** State switching found for each feature
 1318 (firing, storage, sharing) did not align in time. This can be visualized by state switching
 1319 tables, whose different rows graphically represent transitions between global brain
 1320 oscillatory states and firing, storage, and sharing substates. Examples of switching
 1321 tables are shown in (A) for mEC during anesthesia (top) and for mPFC during natural
 1322 sleep (bottom, note the different time scales). Switching tables were neither perfectly
 1323 regular (B, top left), nor random (B, top right), but they were “complex”, displaying
 1324 organized patterns escaping simple description (B, bottom). (C) The complexity of the
 1325 switching tables was larger for THE/REM than for SO/nonREM for most recordings.
 1326 We included two recordings from mPFC under anesthesia for comparison. (D)
 1327 Switching tables were complex in all cases. Complexity values were significantly above

1328 the upper threshold for regularity and below the lower threshold for randomness. (**E**)
1329 The increase of complexity was significant for mEC when transitioning from SO to
1330 THE and for mPFC from nonREM to REM sleep. This trend in CA1 was not
1331 statistically significant (significance assessed in terms of lack of intersection between
1332 95%-confidence intervals and threshold values for both panels **D** and **E**; a (*) symbol
1333 indicates that the number of recordings in this category was not enough to assess
1334 significance but that the median value lied below or above the considered threshold).

1335 **Supplementary figures**



1336

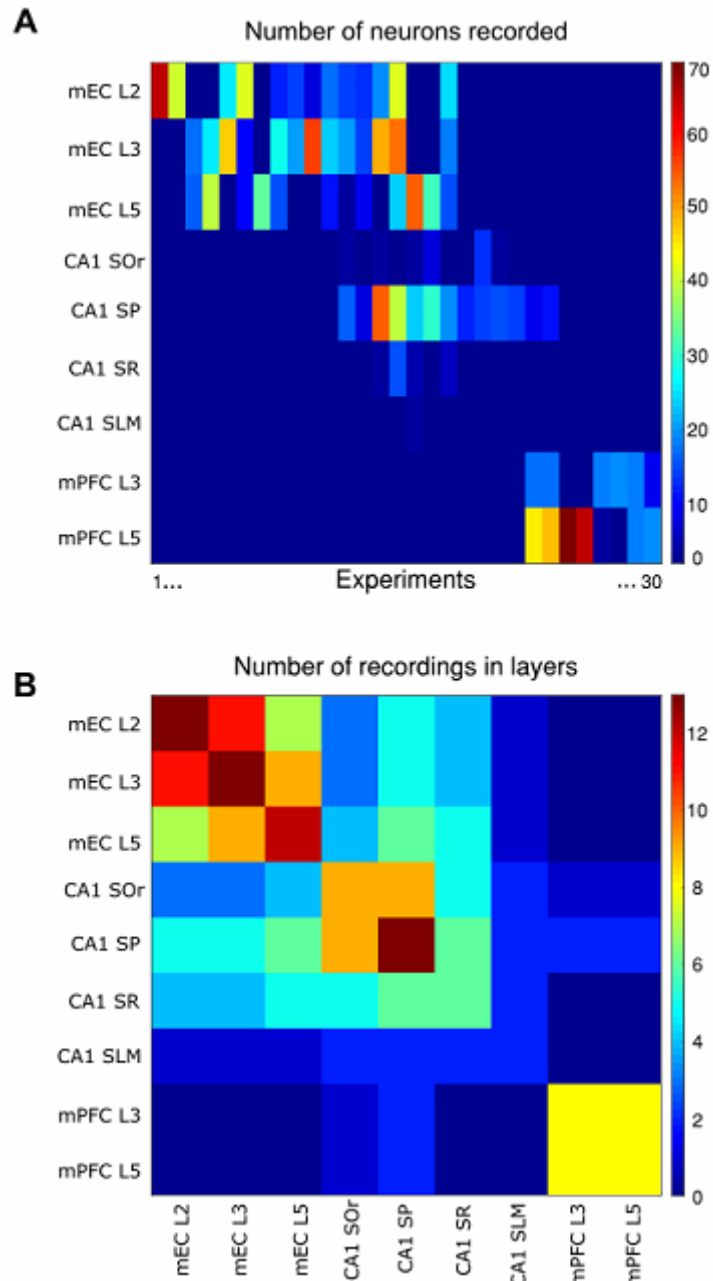
1337 **Figure S1. Recording paradigm.** Schematic representation of the (A) simultaneous
1338 mEC/HPC recording setup and (B) simultaneous mPFC/HPC during anesthesia and
1339 natural sleep. The Nissl stained sections display the anatomical regions recorded by the
1340 different silicon probes used (yellow boxes). Arrows represent the anatomical
1341 connectivity (●: source layer, →: target layer) between the dorsal hippocampus CA1

1342 region (SO: stratum oriens; SP: stratum pyramidale; SR: stratum radiatum; SLM:

1343 stratum lacunosum moleculare) with the dorso-medial entorhinal cortex (mEC, layers I

1344 to VI) and medial prefrontal cortex (mPFC, layers I to VI).

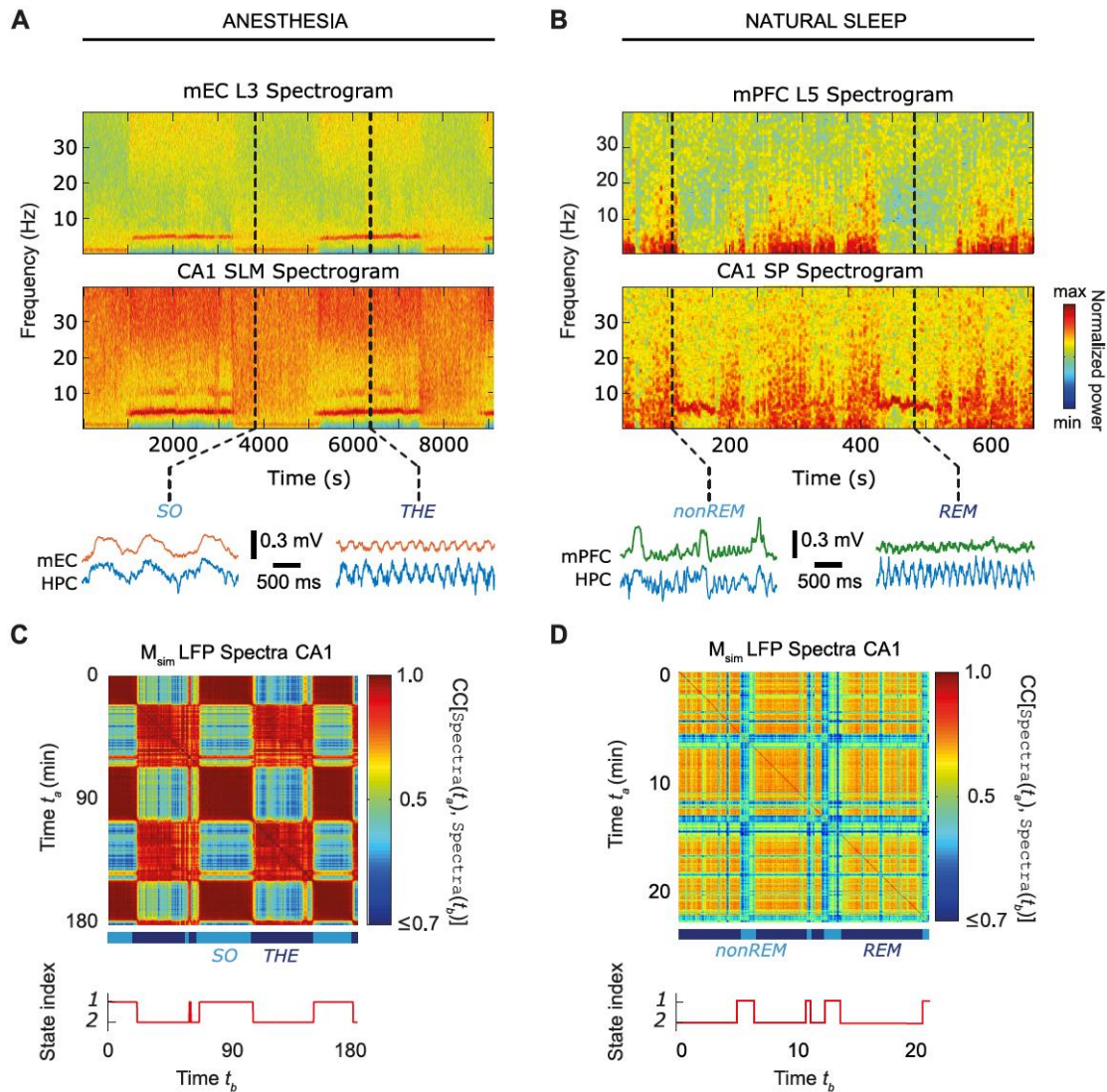
1345



1346

1347

1348 **Figure S2. Information about recordings.** We analyzed data from 30 different
1349 recordings performed in 24 different rats. In each recording we identify single units in
1350 different anatomical locations. **(A)** Number of recorded single units (color coded on the
1351 right scalebar) per anatomical layer (rows), for each of the 30 recordings (columns). **(B)**
1352 Number of recordings (color coded on the right scalebar) simultaneously targeting pairs
1353 of two different anatomical layers.

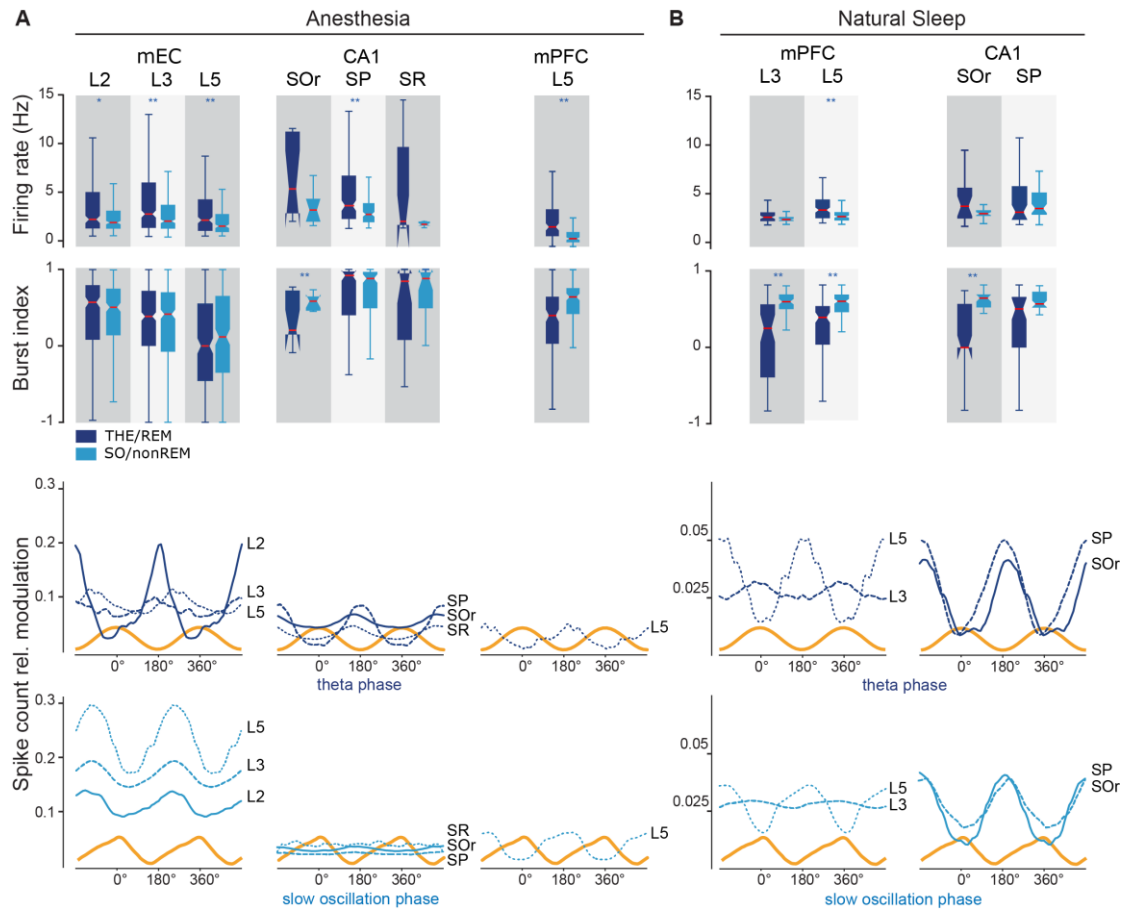


1354

1355 **Figure S3. Global brain oscillatory states.** We performed a time-frequency spectral
 1356 analysis of the LFP signals from all channels. Time-frequency spectrograms of LFPs
 1357 are shown in (A) from mEC III and CA1 SLM layers during anesthesia and in (B) for
 1358 mPFC layer V and CA1 SP. A characteristic alternation is visible between epochs
 1359 dominated by SO/THE rhythms and REM/nonREM. Example LFP traces at time points
 1360 corresponding to the dashed vertical lines are magnified and shown below the
 1361 spectrograms. To characterize global oscillatory states in an unsupervised manner
 1362 within each time-window of analysis (Figure 1), we averaged the power across different
 1363 frequency bands and compiled all LFP channels into the feature vector $Spectra(t)$.
 1364 The similarity matrices corresponding to (A) and (B) are shown in (C) and (D),

1365 respectively. The alternation between SO and THE epochs in **(C)** and between nonREM
1366 and REM epochs in **(D)** is well visible in the marked block structure of the feature
1367 similarity matrices. Unsupervised clustering identified 2 states under anesthesia or
1368 natural sleep.

1369



1370

1371

Figure S4. Effects of global states on unit firing. Transitions between global

1372

oscillatory states in both anesthesia and sleep significantly modulated the median firing

1373

rate in mEC, mPFC and CA1 layers (**A**, top). Burstiness (**B**, bottom) was significantly

1374

modulated during natural sleep only. Both firing rate and bursting indices were

1375

heterogeneous across neurons, as emphasized by long box-plot whiskers. Single units

1376

in mEC, mPFC and CA1 layers fired preferentially at well-defined phases of the

1377

ongoing theta (**B**, top) and slow oscillation (**B**, bottom) rhythms as visualized by phase-

1378

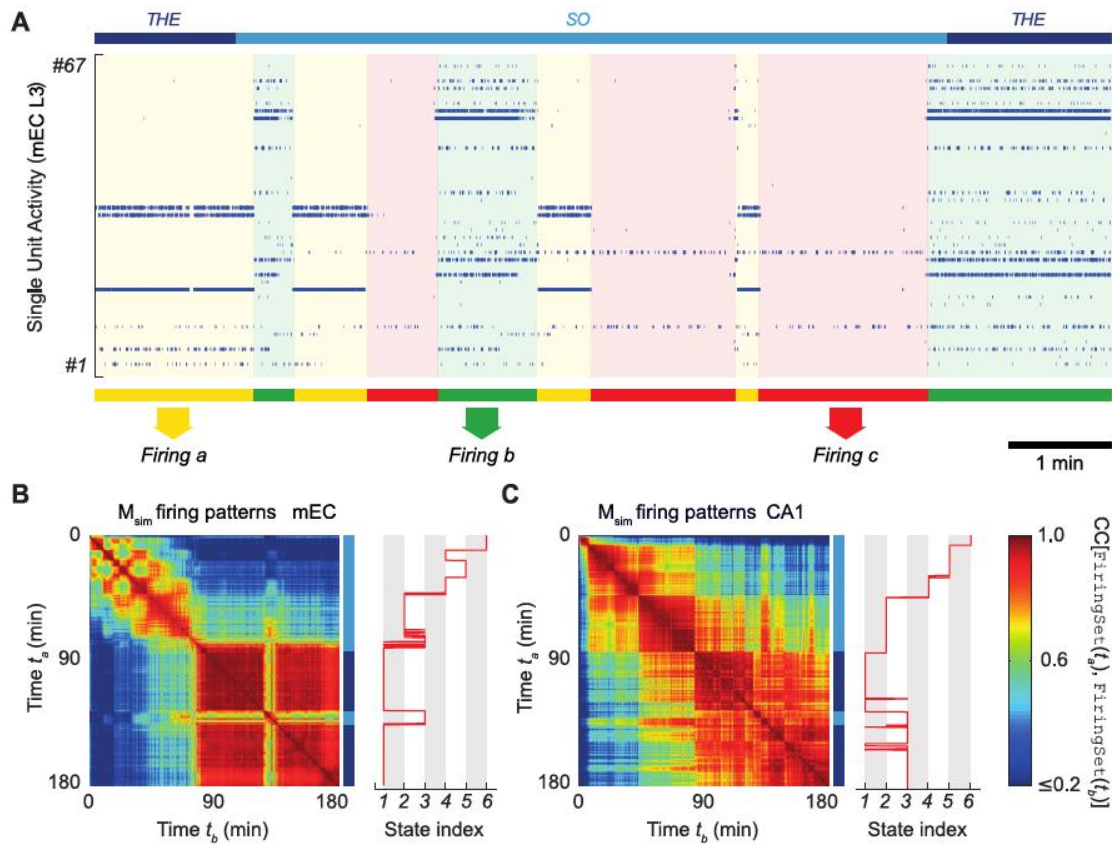
binned histograms of spike count relative modulation, compared with reference average

1379

LFP waveform cycles. Note that phase modulations were an order of magnitude

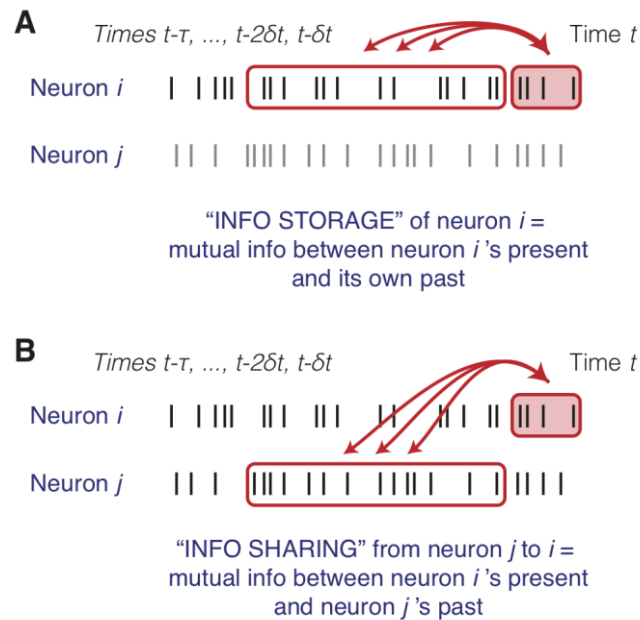
1380

stronger during anesthesia than natural sleep.



1381

1382 **Figure S5. Firing substates.** (A) displays the firing, represented by blue dots, of 67
 1383 neurons recorded in layer 3 in mEC. The solid lines above indicate the global brain
 1384 states (THE and SO) identified using unsupervised clustering of the spectral features of
 1385 the field potential (as described in Figure S3). Unsupervised clustering identified three
 1386 sets of co-firing neurons (indicated by yellow, green and red solid lines), which are
 1387 clearly visible, during the recording time shown here. Note the alternation of the firing
 1388 substates, and the fact that global oscillatory state transitions (THE→SO→THE) do not
 1389 correspond to transitions between firing substates. Below, (B) and (C) represent the
 1390 dynamics of firing sets in mEC and CA1 during the whole recording session, where
 1391 squares across the diagonal represent different firing substates, as in (A).



1392

1393 **Figure S6. Primitive operations in information processing: explanatory cartoons.**

1394 The information conveyed by the activity of a unit at a given time may have different

1395 sources. A fraction of the total information conveyed at time t by a neuron i may have

1396 already been present in i ’s past activity (**A**). Therefore, we say that this fraction of

1397 information is being *actively stored* into neuron i by its activity, implementing a

1398 “memory buffer”. The involvement of a unit into this primitive information processing

1399 operation is quantified by its Active Information Storage score (see Figure 3). A

1400 complementary fraction of the total information conveyed at time t by a neuron i may

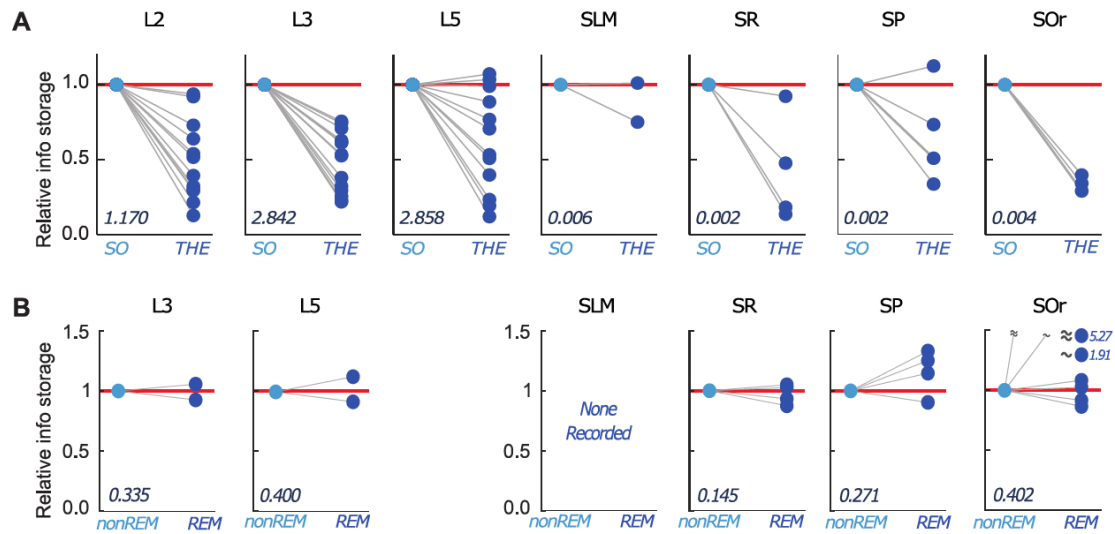
1401 have been present already into the past activity of a different neuron j (**B**). We say in

1402 this case that this fraction of information is *shared* from j toward i , with time-lagged

1403 mutual information providing a pseudo-directed measure of functional connectivity

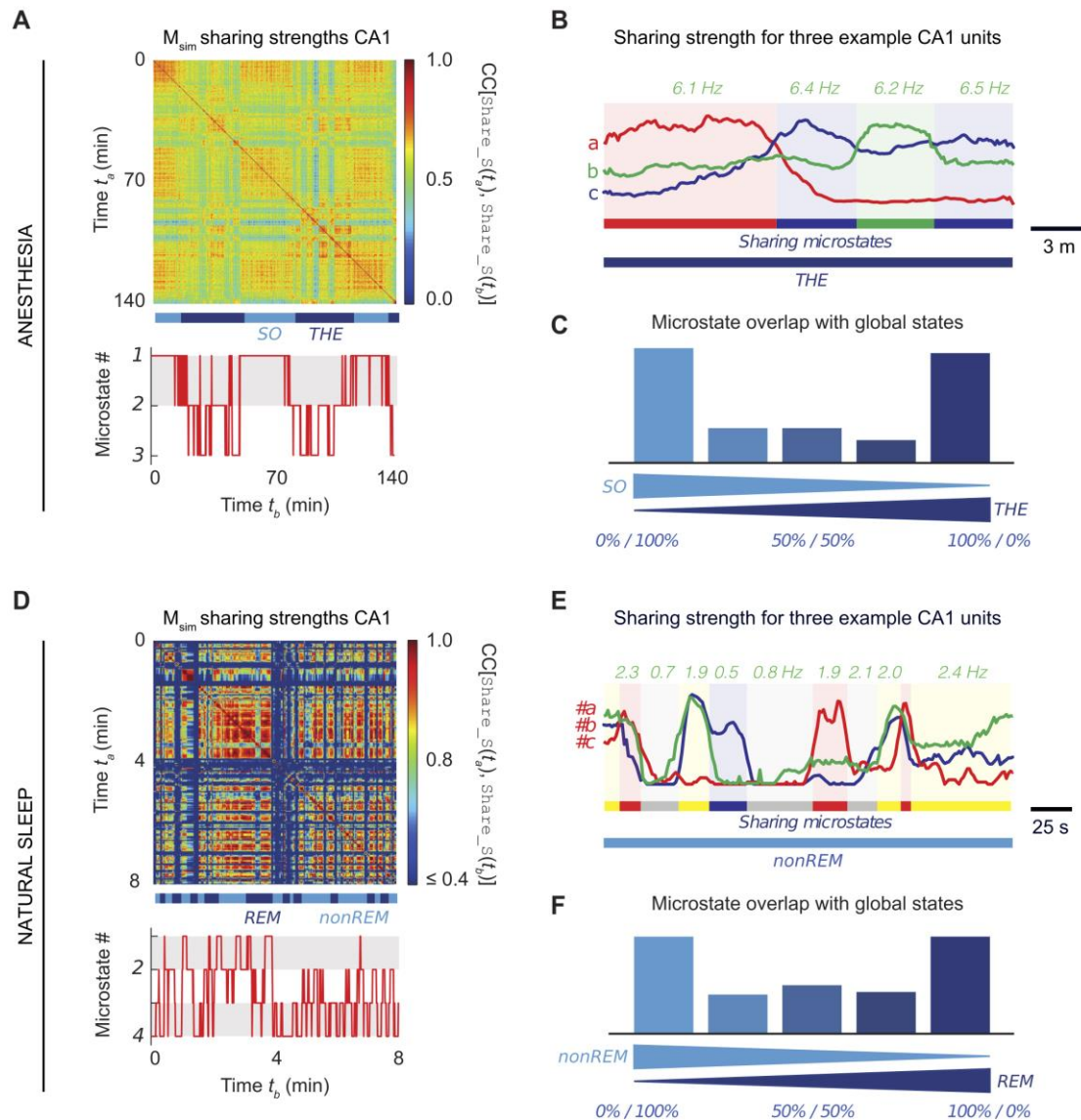
1404 (see Figure 4).

1405



1406

1407 **Figure S7. Information storage is brain state-dependent.** (A) Relative variation of
 1408 active information storage values in the different mEC and CA1 layers between SO and
 1409 THE states during anesthesia. Different lines correspond to different rats. All values are
 1410 normalized to SO values for better visualization of the size and direction of effects. The
 1411 absolute values of active information storage during SO are indicated in the lower left
 1412 corner of each subpanel. During anesthesia, mEC layers have larger active information
 1413 storage values than CA1 layers. Generally, switching from SO to THE state tends to
 1414 reduce active information storage values. (B) Same as A but for mPFC and CA1 layers
 1415 during natural sleep. The active information storage has the same order of magnitude
 1416 for mPFC and CA1 but is lower than mEC during anesthesia. Furthermore, during
 1417 natural sleep there is no major general difference between REM and nonREM (as
 1418 opposed to SO/THE in A).



1419

1420 **Figure S8. Substates of information sharing: additional information.** We show here

1421 additional typical feature similarity matrices M_{sim} obtained from sharing strengths

1422 $Share_S(t)$ in CA1 during anesthesia (**A**) and natural sleep (**D**) (see also Figure 4).

1423 As in firing and storage substates, (**C**) and (**E**) show that the participation of different

1424 neurons to the information sharing was varying along time in a switching fashion

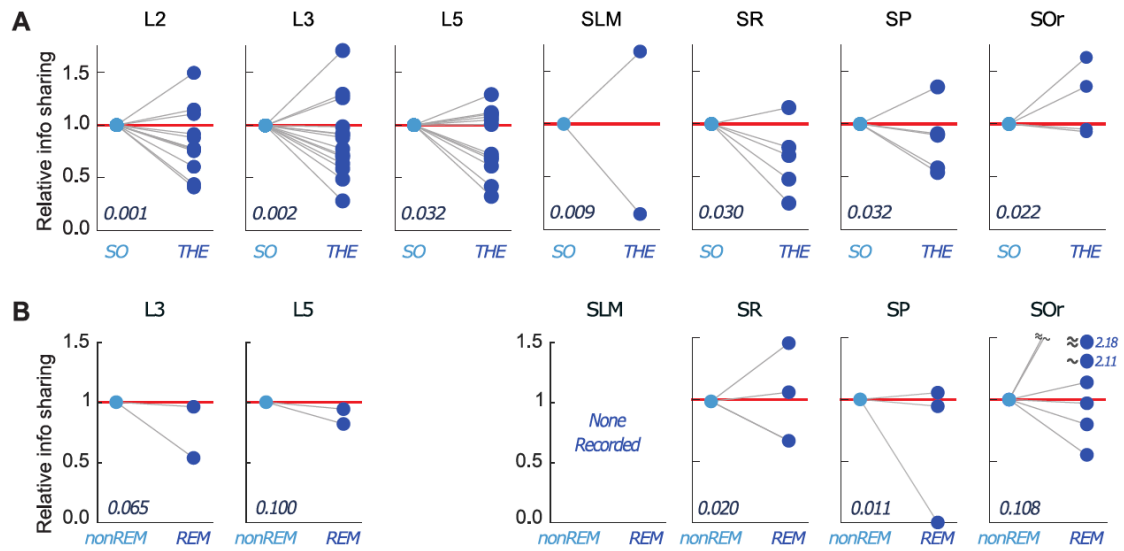
1425 (arbitrary normalized units, smoothed time-series). The values reported above the plots

1426 correspond to the average firing rate of the neuron b (green color) during the

1427 corresponding epochs within consistent sharing substates. Sharing substates tended to

1428 occur during a preferred global oscillatory substate, as indicated by the bimodal
1429 histograms in **(C)** for anesthesia and **(F)** for natural sleep (see also Figure 4D).

1430



1431

1432 **Figure S9. Variations of information sharing as a function of the global brain**

1433 **oscillatory states. (A)** Relative percent variation of information sharing total strength

1434 values between SO/THE states during anesthesia, averaged over different layers in

1435 mEC and CA1. Different lines correspond to different rats and average values of sharing

1436 strength in SO state are normalized to allow a simpler comparison of the size and

1437 direction of effects for different layers, but absolute values of sharing strength in the

1438 SO state, averaged over the different rats, are indicated in the lower left corner of each

1439 subpanel. **(B)** Same as above but for different mPFC and CA1 layers during natural

1440 sleep. We did not observe any systematic direction of change for sharing strengths when

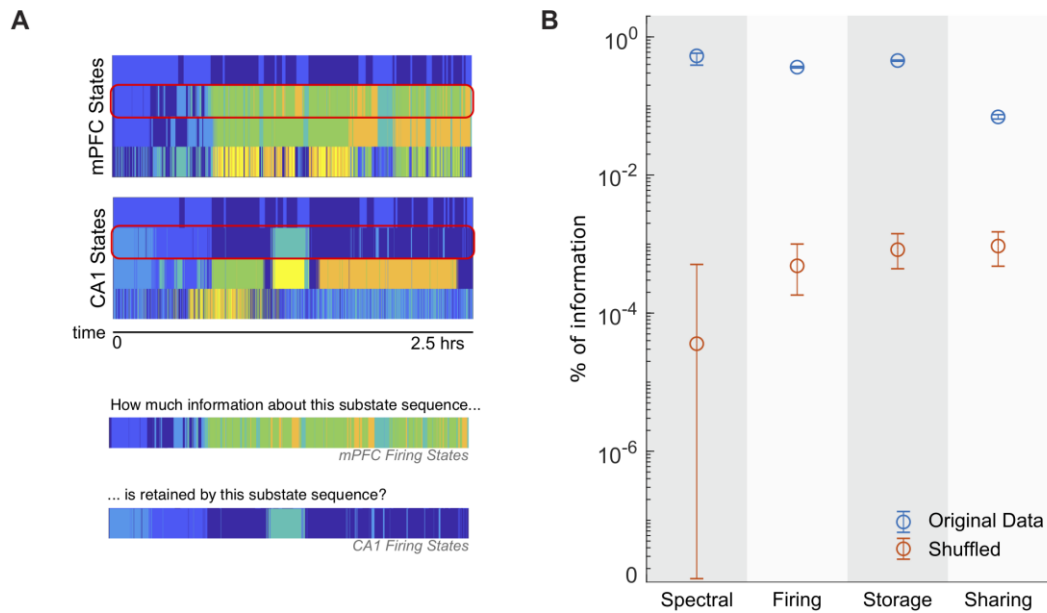
1441 switching from SO to THE states during anesthesia or from nonREM to REM during

1442 natural sleep. mEC layers II and III during anesthesia were associated to the weaker

1443 absolute values of sharing strengths and mPFC layer IV and CA1 SO during natural

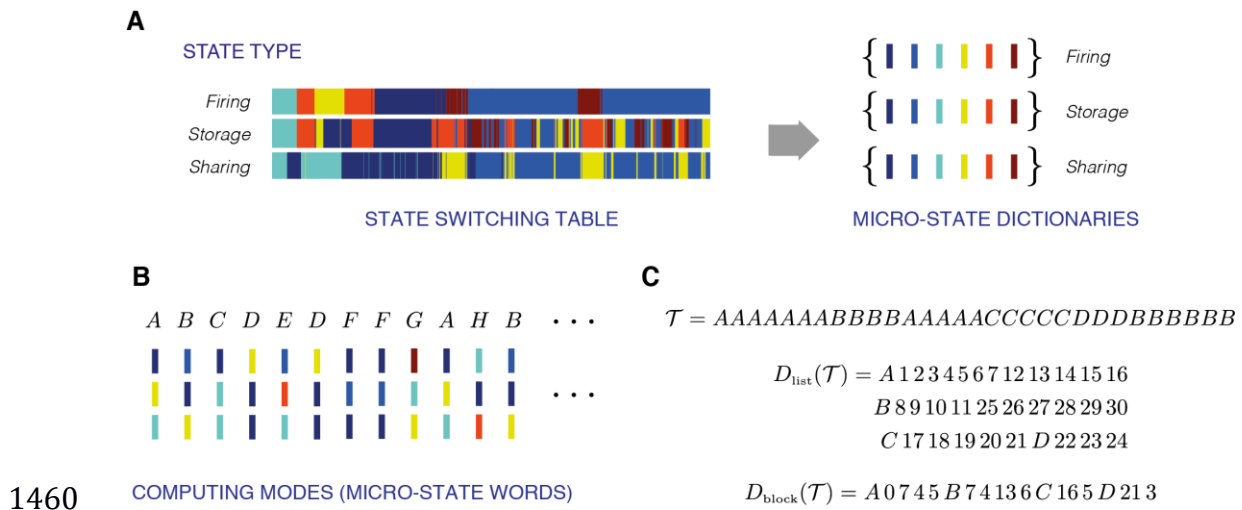
1444 sleep to the stronger values.

1445



1446

1447 **Figure S10. Coordination of substate transitions between brain regions.** Sequences
1448 of firing, storage and sharing substates do not show a perfect match between
1449 simultaneously recorder regions, as visible from the state transition tables of a
1450 representative simultaneous CA1/mPFC recording during natural sleep (**A**, top). To
1451 quantify the level of interregional coordination between substate transitions we
1452 evaluated the mutual information between matching substate sequences in the two
1453 simultaneously probed regions (**A**, bottom). We also estimated the corresponding
1454 chance levels of coordination, by repeating the same procedure on shuffled state
1455 transitions sequences. For all features, we find that the sequences are loosely coupled
1456 between regions, but still far above chance level (**B**). Vertical bars denote the 99%
1457 confidence interval (bootstrap with replacement for original data, permutation-based
1458 for shuffled data, 1000 replicas in both cases). This specific graph is built using the
1459 example in (**A**).



1460

1461 **Figure S11. Calculation of complexity of the state switching table. (A)** A given

1462 recording can be represented by the superposition of 3 sequences of substates for each

1463 feature (firing, storage, sharing). **(B)** At any point in time, the triplet of substates can be

1464 represented as a *word* made of three substate *letters*. For simplicity, the *letters* are color-

1465 coded, and a *word* is represented by a letter from the alphabet (A, B, C etc.). **(C)** A state

1466 switching table \mathcal{T} is the temporal sequence of *words* with one word per analysis window

1467 t_A as defined in Figure 1). There are two ways to represent the sequence of *words*.

1468 $D_{\text{list}}(\mathcal{T})$ lists the positions at which the *words* appear (e.g. at window 1, 2, 3, 4, 5, 6, 7,

1469 12, 13, 14, 15, 16...). This representation is exhaustive, but not compact. $D_{\text{block}}(\mathcal{T})$ lists

1470 how many positions one should skip from the start of the sequence before writing and

1471 in how many consecutive positions the considered *word* should be printed. In the

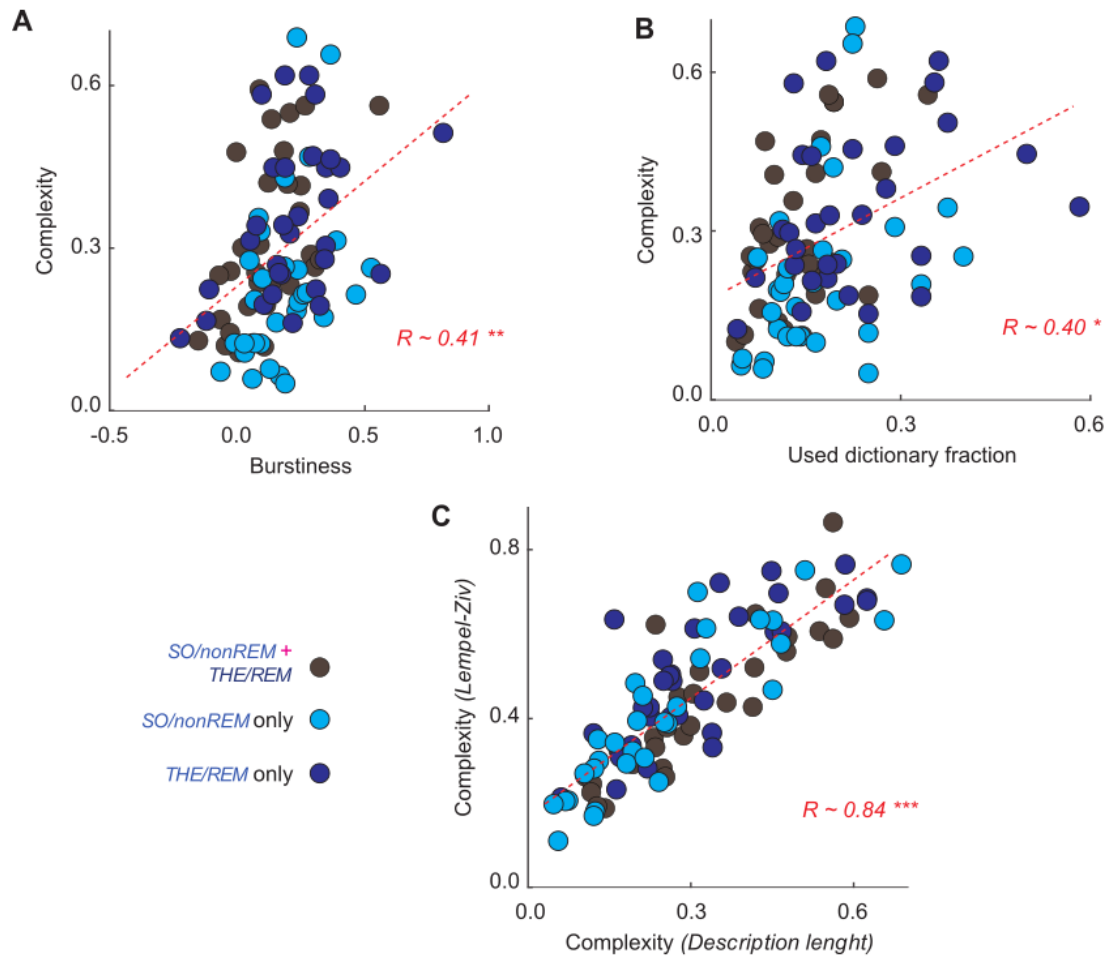
1472 example shown here, the *word* “A” occurs at the beginning of the string – zero positions

1473 skipped – and is then printed seven times. After, 4 positions are skipped, and it is written

1474 again 5 times, etc. This representation is more compact. Complexity is given by the

1475 ratio between the lengths of the descriptions $D_{\text{block}}(\mathcal{T})$ and $D_{\text{list}}(\mathcal{T})$.

1476



1477

1478 **Figure S12. Burstiness and Used Dictionary Fraction explain complexity.**

1479 Complexity linearly increased with burstiness (A) and Used Dictionary Fraction (B).

1480 (C) Lempel-Ziv (LZ) complexity as a function of our measure of complexity. The two

1481 complexities were highly linearly correlated, and results of complexity analyses were

1482 thus qualitatively the same using either one of the two measures. We plot together

1483 results for complexity analyses restricted to SO/nonREM states (light blue dots), to

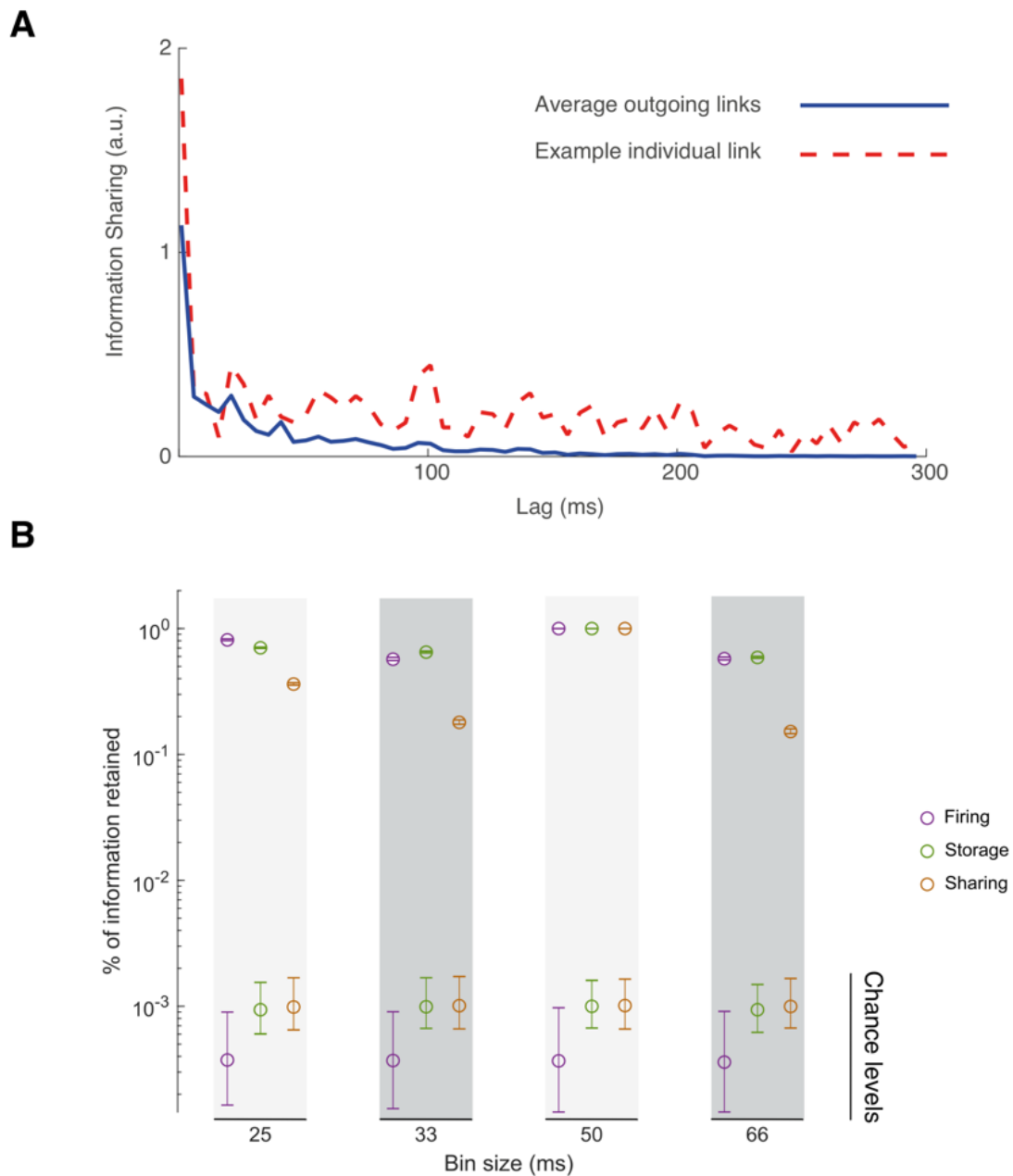
1484 THE/REM states (dark blue dots) or over all states combined (grey dots), as no

1485 significant differences were observed between the three groups with respect to the

1486 plotted linear trends.

1487

1488



1489

1490 **Figure S13. Additional robustness analyses.** (A) Lagged mutual information terms
1491 between spike trains, the building block terms of both storage and sharing features,
1492 quickly decay as a function of the considered lag τ , justifying our choice to integrate
1493 MI only for latencies up to an average theta cycle period ($\sim 125 - 250$ ms depending on
1494 recordings). The red dashed line refers to a representative individual link, associated to
1495 a specific pair of units, and show some additional peak. However, these secondary
1496 peaks are much smaller than the main peak for very short latency and are not aligned
1497 for different pairs of units so that they are averaged out away when averaging over

1498 multiple outgoing links originating from a same unit (solid blue line). **(B)** Our procedure
1499 for substate extraction is robust against changes of the bin size. We considered four
1500 different choices of bin size different from the original choice of 50 ms, extracted
1501 substate sequences for each of these new bin choices and computed mutual information
1502 between the newly obtained and the original corresponding substate sequences. Shown
1503 here are the relative fraction of retained information for different bin sizes and substate
1504 types (evaluated on a representative recording, mPFC, natural sleep, the same as for
1505 figure S10). Across all features, the fraction of information retained about the substate
1506 sequences for the main reference bin size of 50 ms is two orders of magnitude above
1507 chance levels, with sharing being most effected. Vertical bars denote 99% confidence
1508 interval (bootstrap with replacement for original data, permutation-based for shuffled
1509 data, 1000 replicas in both cases).

1510
1511

1512 **Supplementary tables**

1513

1514 *Table S1 – Percent of information about substate sequences in empirical*
1515 *recordings retained after shuffling*

Substate	Anesthesia	Natural Sleep
Spectral	2.55×10^{-9} , 1.58×10^{-4}	1.47×10^{-8} , 5.43×10^{-4}
Firing	6.13×10^{-5} , 5.71×10^{-4}	9.78×10^{-5} , 5.71×10^{-4}
Sharing	4.68×10^{-4} , 1.13×10^{-3}	2.66×10^{-4} , 1.42×10^{-3}
Storage	9.49×10^{-4} , 1.15×10^{-3}	4.15×10^{-4} , 1.61×10^{-3}

1516 *0.1% and 99.9% percentile of MI/H for state sequences. The very low values of these*
1517 *amounts of relative information indicate that the observed state sequences strongly*
1518 *deviate from a null hypothesis of lack of temporal structure*